Journal of Alloys and Compounds 857 (2021) 157467

Contents lists available at ScienceDirect

Journal of Alloys and Compounds

journal homepage: http://www.elsevier.com/locate/jalcom

Effect of off-stoichiometric compositions on microstructures and phase transformation behavior in Ni-Cu-Pd-Ti-Zr-Hf high entropy shape memory alloys

D. Piorunek [a, 1, *], O. Oluwabi [a], J. Frenzel [a, 2], A. Kostka [b], H.J. Maier [c], C. Somsen [a], G. Eggeler [a]

[a] Institut für Werkstoffe, Ruhr-Universität Bochum, Universitätsstr. 150, 44801 Bochum, Germany
[b] Zentrum für Grenzflächendominierte Höchstleistungswerkstoffe (ZGH), Ruhr-Universität Bochum, Universitätsstr. 150, 44801 Bochum, Germany
[c] Institut für Werkstoffkunde (Materials Science), Leibniz Universität Hannover, An der Universität 2, 30823 Garbsen, Germany

ARTICLE INFO

Article history:
Received 18 May 2020
Received in revised form
11 August 2020
Accepted 5 October 2020
Available online 6 October 2020

Keywords:
High entropy alloy
Shape memory alloy
Alloy design
Martensitic transformation
Thermodynamic constitution
Microstructure

ABSTRACT

High entropy shape memory alloys (HE-SMAs) show reversible martensitic phase transformations at elevated temperatures. HE-SMAs were derived from binary NiTi, to which the elements Cu, Pd, Zr and Hf are added. They represent ordered complex solid solutions. Their high temperature phase is of B2 type, where the added elements occupy sites in the Ni-(Cu, Pd) and Ti-sub-lattices (Zr, Hf). In the present study, advanced microstructural and thermal characterization methods were used to study the effects of the additional alloy elements on microstructures and phase transformations. The ratios of Ni-equivalent (Ni, Cu, Pd) and Ti-equivalent (Ti, Zr, Hf) elements in HE-SMAs were varied to establish systems that correspond to stoichiometric, under- and over-stoichiometric binary alloys. It is shown that basic microstructural features of cast and heat-treated HE-SMAs are inherited from the nine binary X–Y subsystems (X: Ni, Cu, Pd; Y: Ti, Zr, Hf). The phase transition temperatures that characterize the martensitic forward and reverse transformations depend on the concentrations of all alloy elements. The data obtained demonstrate how martensite start temperatures are affected by deviations from the composition of an ideal stoichiometric B2 phase. The findings are discussed in the light of previous work on the concentration dependence of SMA transformation temperatures, and directions for the development of new shape memory alloy compositions are proposed.

1. Introduction

Shape memory alloys (SMAs) are functional materials that exhibit fascinating properties [1–7]. They are able to re-establish their geometry after deformations which significantly exceed reversible elastic strains that are tolerated by conventional metallic engineering materials. Depending on alloy composition and microstructure, two different types of shape memory effects can be exploited [1,8,9]. The thermal shape memory effects (one way and two way effects) are activated by temperature changes. In contrast, the mechanical shape memory effect (pseudoelasticity) occurs when the initially austenitic material, where sufficiently high stresses cause large deformations associated with a stress-induced formation of martensite, is unloaded. Both types of shape memory effects rely on a reversible martensitic phase transformation, which can be thermally and mechanically triggered [10].

Recently, SMAs with a complex alloy chemistry, referred to as high entropy shape memory alloys (HE-SMAs), have been introduced as a new class of materials [11–13], and they receive increased scientific attention at present [14–21]. In the light of ongoing research on conventional structural high entropy alloys (HEAs) [22–26], researchers became curious about how chemical complexity affects crystal structures that can undergo martensitic transformations and how this alters elementary transformation processes and functional SMA properties. Early results obtained for HE-SMAs suggest that they have relatively high transformation temperatures, which rendered them attractive as novel high temperature shape memory alloys [11,15,27]. Firstov et al. [11–13] were

* Corresponding author.
E-mail address: david.piorunek@rub.de (D. Piorunek).
[1] https://orcid.org/0000-0001-5096-8835
[2] https://orcid.org/0000-0002-2778-5392

https://doi.org/10.1016/j.jallcom.2020.157467

the first to introduce HE-SMAs as a new material class derived from binary NiTi, the commercially most successful SMA [1]. The high temperature phase, austenite, in both binary NiTi and multinary HE-SMAs has a B2 crystal structure, where Ni and Ti atoms occupy separate sub-lattice sites [21,28]. In binary NiTi, the low temperature phase, martensite, has a B19' structure [21,28]. Firstov et al. [11–13] have demonstrated that Cu, Co, Zr and Hf substitute Ni and Ti in their respective sub-lattices. Similar to conventional HEAs [22–26], equimolar concentrations of elements occupying specific sub-lattices were selected to design HE-SMAs [11]. One important observation made by Firstov et al. [11] was that HE-SMAs exhibit good cyclic stability [11]. It was suggested that similar to what was proposed for HEAs [29,30], the high number of alloy elements results in a strengthening effect, which suppresses irreversibilities related to dislocation mediated plasticity [11]. Grain refinement [31–33], precipitation hardening [34–36] and optimization of the crystallographic compatibility between the lattices of martensite and austenite [37–41] were explored in an effort to improve functional stability. However, in shape memory technology, the possibility of entropy-based solid solution concepts has so far not received significant attention.

In a previous study [21], a first step towards a better understanding of the effects of the number of alloy elements on solidification microstructures and martensitic transformations in HE-SMAs was made. The additional alloy elements were assigned to two groups, reflecting their sub-lattice preferences: the Ni-equivalent elements (Ni, Cu and Pd) and the Ti-equivalent elements (Ti, Zr and Hf). In the following, these two groups will be referred to as Ni_{equ} and Ti_{equ}. It was shown that solidification of HE-SMAs results in the partitioning of individual alloy elements to dendritic and interdendritic regions. However, the compositional ratios between the two groups of elements remained almost constant throughout the microstructure. The effects of alloy compositions on transformation temperatures could be interpreted invoking valence electron concepts. Moreover, martensitic transformations, crystal structures and microstructures in a new NiCuPdTiZrHf HE-SMA were explored [21]. Thermodynamic aspects of this HE-SMA were discussed with respect to the effects of the number of alloy components and ordering phenomena, which are related to the formation of the B2 phase [21].

Previous studies on HE-SMAs, e.g. Refs. [11–13,15,21] focused on equiatomic compositions, which are associated with the highest entropies of mixture [23,25,26] and which were proposed to have a high temperature B2 phase [21,42]. In the present work, the effects of deviations from this ideal equiatomic stoichiometry are explored. This is of particular interest because in conventional Ni-Ti, small deviations from the ideal stoichiometric compositions can have strong effects on microstructures and phase transformations [42–44]. Fig. 1, shows the phase diagram of binary Ni-Ti [45]. Binary Ni-Ti SMAs typically feature compositions close to 50 at.% Ni [1,28], and a composition of 50 at.% Ni and 50 at.% Ti is referred to as the stoichiometric composition. The dashed central area in Fig. 1 indicates the composition/temperature range where the B2 phase is stable. This region narrows down with decreasing temperatures. Fig. 1 shows that solubility limits of the B2 phase are asymmetric, i.e. B2 shows an increasing solubility for Ni with increasing temperature [46]. Even at high temperatures, almost no excess Ti can be solved. The small arrow of length Δx indicates a deviation from the ideal stoichiometric composition. In the present study, both positive and negative deviations Δx from ideal stoichiometry are considered.

The thermodynamic/kinetic nature of the Ni-Ti system provides opportunities for the design of new shape memory alloys. First, quenching of solution annealed Ni-Ti from high temperatures allows freezing in Ni-rich single-phase microstructures. In this

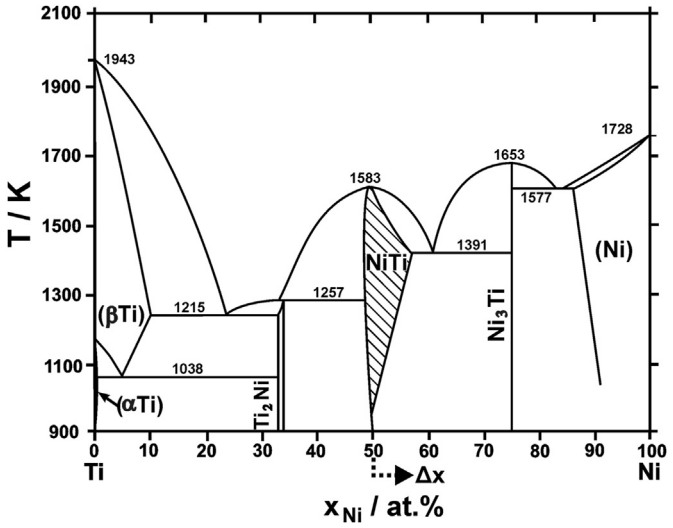

Fig. 1. Binary phase diagram of Ni-Ti (slightly modified from Ref. [45]). The dashed region indicates the single phase B2 regime. Δx characterizes a compositional shift away from the ideal stoichiometry.

metastable state, the Ni-concentration significantly affects phase transformation temperatures [42–44]. An increase of the Ni-concentration by only 0.1 at.% Ni can result in a drop of the martensite start temperature M_S by more than 10 K [42–44]. This dependence of M_S on the Ni concentration [42–44] allows realizing elevated SMA transformation temperatures, e.g. for actuator applications [1,37]. One can also establish low transformation temperatures, which promote pseudoelasticity at room temperature, for example for the use of SMAs for guide wires, stents and other medical applications [1,47,48]. Second, exposing supersaturated Ni-rich Ni-Ti SMAs to temperatures exceeding ≈250 °C, results in precipitation processes. Different types of phases, e.g. Ni_4Ti_3, Ni_3Ti_2 and Ni_3Ti can form [46,49]. The microstructural evolution processes related to aging can affect transformation behavior in a complex manner [50–53]. Most importantly, precipitation results in an increase in phase transformation temperatures and can give rise to multiple-step transformations [50–53]. Aging of Ni-rich NiTi is often applied in shape memory technology to fine tune transformation temperatures and to improve the stability of the shape memory effects [34–36,54]. Third, the microstructures of Ti-rich Ni-Ti alloys consist of two constituents, namely B2 or B19′ (depending on temperature) and of Ti_2Ni. The phase diagram, Fig. 1, suggests that Ti_2Ni forms as a result of a peritectic reaction during solidification [45]. Ti-rich Ni-Ti SMAs have received less attention in science and technology [55,56]. Ti_2Ni is a brittle phase, which promotes early fracture during mechanical loading [56–58].

The present study demonstrates how the evolution of microstructures during processing and the functional properties associated with the martensitic phase transformation are affected when the ratios of Ni_{equ} and Ti_{equ} are varied. Their concentrations $x_{Ni\text{-}equ}$ and $x_{Ti\text{-}equ}$ are obtained by considering all elements that partition to the Ni and Ti sub-lattices of the B2 phase, respectively [21]. Table 1 specifies the alloy compositions that were investigated in the present study, where focus is placed on senary HE-SMAs of type Ni-Cu-Pd-Ti-Zr-Hf, using binary Ni-Ti alloys as reference. Table 1 also introduces abbreviations for the different compositions. Special emphasis is placed on the deviation parameter Δx. This parameter indicates the compositional shift away from the ideal stoichiometry of the B2 phase, Fig. 1. In HE-SMAs, a composition that corresponds to 50 at.% of Ni-equivalent ($x_{Ni\text{-}equ} = 50\%$) and 50% of Ti-equivalent alloy elements ($x_{Ti\text{-}equ} = 50\%$) is referred to as

Table 1
Alloy compositions and abbreviations used for the alloys considered in the present study.

Composition	Abbreviation	$x_{Ni\text{-}equ}$/at.%	Δx/at.%
$Ni_{51}Ti_{49}$	**BinΔx1**	51	1
NiTi	**BinΔx0**	50	0
$Ni_{48.6}Ti_{51.4}$	**BinΔx-1.4**	48.6	−1.4
$Ni_{45}Ti_{55}$	**BinΔx-5**	45	−5
$Ni_{17}Cu_{17}Pd_{17}Ti_{16.333}Zr_{16.333}Hf_{16.333}$	**SenΔx1**	51	1
NiCuPdTiZrHf	**SenΔx0**	50	0
$Ni_{15.833}Cu_{15.833}Pd_{15.833}Ti_{17.5}Zr_{17.5}Hf_{17.5}$	**SenΔx-2.5**	47.5	−2.5
$Ni_{15}Cu_{15}Pd_{15}Ti_{18.333}Zr_{18.333}Hf_{18.333}$	**SenΔx-5**	45	−5
$Ni_{13.333}Cu_{13.333}Pd_{13.333}Ti_{20}Zr_{20}Hf_{20}$	**SenΔx-10**	40	−10
$Ni_{11.667}Cu_{11.667}Pd_{11.667}Ti_{21.667}Zr_{21.667}Hf_{21.667}$	**SenΔx-15**	35	−15

quasi-stoichiometric. Negative Δx values correspond to shifts to the Ti/Ti_{equ}-rich side in the phase diagrams, whereas positive values indicate Ni/Ni_{equ}-rich compositions in Ni-Ti SMAs/HE-SMAs. In the present study, HE-SMAs with quasi-stoichiometric, under and over quasi-stoichiometric compositions were established by applying identical concentration shifts for all elements that belong to one specific group of Ni/Ti-equivalent alloy components, Table 1.

2. Materials and experiments

The different alloy compositions specified in Table 1 were realized with ingots with masses close to 60 g and prepared applying an optimized melting procedure [42,43]. Specifically, high purity raw materials were used as melting feedstock, Table 2. Button shaped ingots were prepared using a laboratory arc melter of type Edmund Bühler AM. The binary and senary ingots were remelted 5 and 15 times, respectively, to ensure sufficient mixing. In each melting/remelting cycle, the material was kept for 20 s in the liquid state. After the final remelting step, cuboidal ingots were drop cast into a water-cooled copper-mold. The microstructures of the different alloys were characterized in the as-cast state and after homogenization at a temperature of 1173 K for 100 h under Argon (99.9999 vol%, slow continuous flow) followed by water quenching.

The microstructures of the different alloys were investigated by scanning electron microscopy (SEM) using a LEO 1530 VP SEM and an energy dispersive X-ray analysis (EDX) system of type EDAX Apollo SDD XV. All SEM micrographs were taken using electron backscatter contrast. The chemical compositions of the different ingots were characterized by EDX, where integration times of 100 s were used. Average compositions of the different ingots were determined by EDX area scans where 150,000 μm^2 regions were probed. In addition, local point analysis was performed for different constituents. The volume fractions of the B2 phase were assessed by evaluating regions of at least 35,000 μm^2 using quantitative image analysis (software: IMS Client from Imagic Bildverarbeitung AG). Metallographic cross sections for SEM/EDX characterization were prepared following cutting, grinding and polishing procedures. Transmission electron microscopy (TEM) analysis was carried out in a FEI Tecnai F20 operating at a nominal acceleration voltage of 200 kV. Diffraction patterns were evaluated using the JEMS software from Pierre Stadelmann [59]. TEM lamella were micromachined using a FEI Helios G4 CX - focused ion beam (FIB) system operated at 30 kV. In the final specimen preparation step, low voltage (5 kV) ion-beam cleaning was applied for 2 min on each side of the TEM sample, in order to keep FIB beam damage at a minimum. The phase transformation behavior of homogenized samples was analyzed by differential scanning calorimetry (DSC) in the temperature range between 123 and 873 K. A DSC instrument of type Netzsch A 204 F1 Phoenix was used, applying a heating/cooling rate of 10 K/min under an Ar flow. Samples for DSC analysis were prepared by low speed cutting and mild grinding/polishing. Further details on DSC analysis and sample preparation are given elsewhere [42,43].

Table 2
Chemical purity, geometry and supplier of feedstock.

Elements	Purity/wt.%	Geometry	Supplier
Ni	≥99.995	Pellets	Chempur GmbH
Cu	≥99.99	Pellets	Ampere GmbH
Pd	≥99.95	Granules	Gemsmart GmbH
Ti	≥99.995	Plates	HMW Hauner GmbH
Zr	≥99.95	Crystal bars	SCMG Europe GmbH
Hf	≥99.95	Crystal bars	SCMG Europe GmbH

3. Results

3.1. Binary NiTi

Fig. 2 presents microstructures of binary Ni-Ti with stoichiometric, over- and under-stoichiometric Ni-concentrations. The SEM micrographs were obtained from heat-treated samples. No significant differences were observed between as-cast (not shown here) and heat-treated material states. The stoichiometric NiTi alloy, Fig. 2a, shows a fully martensitic microstructure with only a few secondary phase particles of type TiC and oxygen-stabilized Ti_2Ni [43,60]. Their presence is due to the impurity content of the alloy. They are not important for the objectives of the present study. A Δx-shift of +1 at.% yields the microstructure presented in Fig. 2b. The corresponding material is in the fully austenitic state and no martensitic microstructural features are present. This is in line with what is expected, since this type of alloy composition has a M_S temperature below room temperature [42,43]. Again, only a few impurity-related secondary phases are present. A Δx-shift of 5 at.% towards the Ti-rich side of the phase diagram results in microstructures which contain two constituents, Fig. 2c. EDX analysis shows that the dark regions in Fig. 2c have a Ni/Ti ratio close to 1:2, which suggests that it represents Ti_2Ni, in line with previous TEM observations [43]. This dark phase sprawls between irregular shaped martensite islands. The formation of this type of microstructure is also expected based on literature [61].

3.2. As-cast senary alloys

The microstructures of the as-cast senary Ni-Cu-Pd-Ti-Zr-Hf HE-SMAs are significantly more complicated, Fig. 3. The SEM micrographs, Fig. 3, reveal large scale chemical heterogeneities related to solidification partitioning [21]. The volume fractions of the different microstructural constituents depend on the size of Δx (compositional deviation from quasi-stoichiometry, Fig. 1). The HE-SMA with equimolar composition, Fig. 3a, shows a seaweed type of

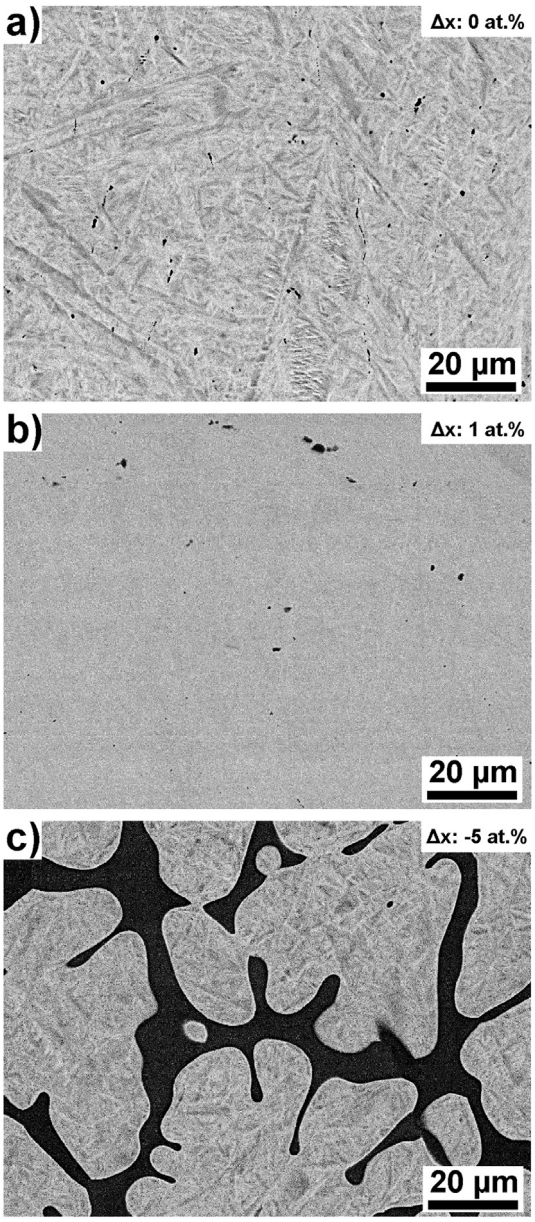

Fig. 2. SEM backscatter micrographs of heat-treated binary Ni-Ti alloys with different compositions: (a) Stoichiometric NiTi (x_{Ni} = 50.0 at.%). (b) Over-stoichiometric NiTi (x_{Ni} = 51.0 at.%). (c) Under-stoichiometric NiTi (x_{Ni} = 45.0 at.%).

microstructure, which has recently been described [21]. The material mainly consists of B2 and/or B19′ (phases which can undergo the martensitic transformations) [21]. Adding 1 at.% of Ni-equivalent elements to this alloy results in the formation of additional particles, Fig. 3b. These are shown at a higher magnification in the inset in Fig. 3b. Different microstructures were observed for Ni-Cu-Pd-Ti-Zr-Hf alloys with Ti_{equ}-rich compositions, i.e. for alloys with negative deviation Δx, Fig. 3 c-f. These material states consist of several phases, which feature different grey levels in the SEM images. The volume fractions of these phases are significantly affected by Δx. The microstructures of SenΔx-2.5 and SenΔx-5 are dominated by cell-like structures, where bright irregularly shaped islands are separated by dark regions, Fig. 3c and d. The lighter grey phase shows martensitic plate/needle-like features. It seems reasonable to assume that this microstructure represents B19′ martensite. The latter is embedded into a dark appearing network, where small bright particles are aligned, Fig. 3d. A further shift of the Δx value to −10 at.% results in the formation of a third microstructural component consisting of large elongated particles, Fig. 3e. These particles often contain cracks. The SenΔx-10 alloy still shows islands of martensite, separated by a dark matrix with small particles. Finally, Fig. 3f presents the microstructure of the alloy with the largest negative Δx-shift of −15 at.%. In this alloy, only very small amounts of martensite were found. The corresponding microstructure mainly consisted of large bright elongated particles, embedded in a darker matrix with an aligned particle network, where particles have diameters in the sub-µm range.

3.3. Microstructures of heat-treated senary alloys

Fig. 4 shows the microstructures of the different HE-SMAs after homogenization annealing at 1173 K for 100 h. An effort was made to classify the different microstructural constituents, which are labeled as I, II, III, IV and V, according to their chemical composition and morphology. The microstructures of the annealed material states differ from those of the as-cast alloys. Small particle populations in the as-cast state coarsen during homogenization annealing. Microstructures are still heterogeneous after homogenization annealing, but to a much lesser extent than after casting. Most importantly, no significant chemical gradients are detected within the individual microstructural constituents. The quasi-stoichiometric alloy consists of martensite, Fig. 4a. In a previous study, its crystal structure was identified as B19′ [21], in line with what is known for binary NiTi [28]. The HE-SMA with a Δx value of +1.0 at.% consists of an austenitic matrix (constituent I) and particles (constituent II) with sizes of up to 10 µm, showing a large contrast, Fig. 4b (not detected in the as-cast state, Fig. 3b). The microstructures of the alloys with Ti_{equ}-rich compositions, Fig. 4 c-f, show similar microstructural constituents as observed in the as-cast HE-SMAs, Fig. 3. In the SenΔx-2.5 and SenΔx-5 alloys, the microstructural constituent I (now martensite), a dark continuous phase (constituent III), and small particles of a third phase (constituent IV) were detected (highlighted by arrows in the high magnification insets of Fig. 4c and d). Constituent II is not present in Ti_{equ}-rich HE-SMAs. With further increasing Ti_{equ} compositions, Fig. 4d–f, the volume fraction of martensite (constituent I) decreases, whereas the fraction of the other phases increases. In case of the HE-SMAs with Δx-shifts of −10 and −15 at.%, Fig. 4e and f, large elongated shaped particles are present (constituent V). Only small amounts of constituent I are observed for the alloy with the highest degree of off-stoichiometry, Fig. 4f. The microstructure of this material almost exclusively consists of phases III, IV and V which all can be easily recognized by their morphologies, respective brightness, and by the presence of needle/plate-like martensite patterns. The latter is difficult to see in the overview images of Fig. 4 but is clearly resolved in Fig. 5, which presents a higher magnification micrograph of SenΔx-10, with microstructural constituents I, III, IV and V. Phase V shows characteristic plate- or needle-like features, which are very similar to what is observed for microstructural constituent I. These features were observed for most (not all) phase V particles in SenΔx-10 and SenΔx-15 alloys.

3.4. Volume fractions of microstructural constituents

Quantitative image analysis was used to evaluate how the volume fraction of constituent I depends on the off-stoichiometry in binary and senary SMAs, Fig. 6. In line with the binary phase diagram shown in Fig. 1 and previous reports in literature [28,43,45], Fig. 6 reveals that binary Ni-Ti alloys have a certain solubility for excess Ni, while there is no significant solubility for excess Ti. In

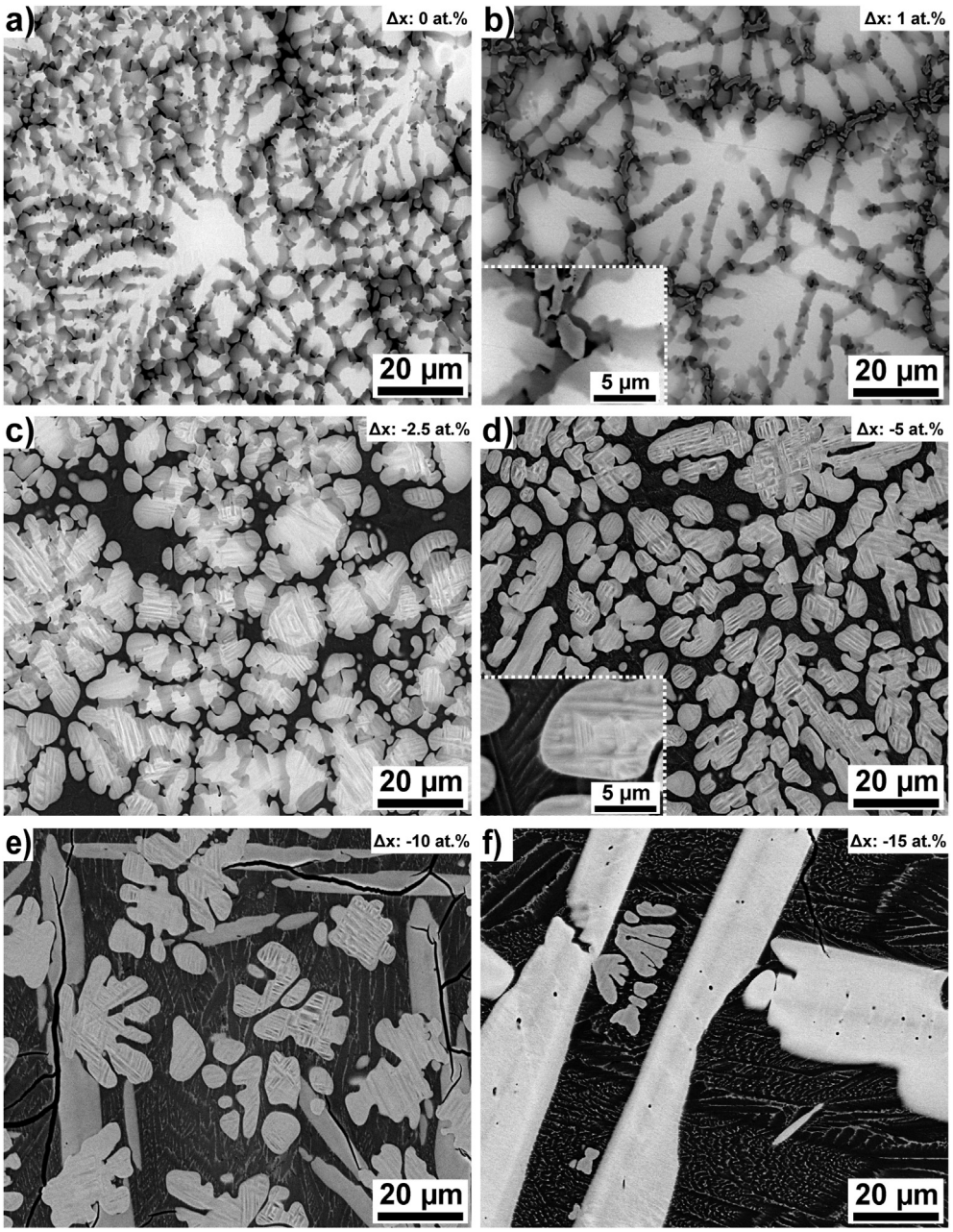

Fig. 3. SEM backscatter micrographs of as-cast Ni-Cu-Pd-Ti-Zr-Hf alloys with different compositions: (a) Stoichiometric composition (Δx = 0 at.%). (b) to (f): Positive and negative deviations Δx from ideal stoichiometry: (b) Δx = 1 at.%, (c) Δx = −2.5 at.%, (d) Δx = −5 at.%, (e) Δx = −10 at.% and (f) Δx = −15 at.%.

contrast, the senary systems do not show significant solubility for excess atoms, neither for Ni- nor for Ti-equivalent elements. Compositional shifts in both directions result in a decrease of the volume fraction of microstructural constituent I (austenite or martensite). Both alloy systems, binary Ni-Ti and Ni-Cu-Pd-Ti-Zr-Hf, exhibit similar volume fractions of constituent I for Ti/Ti_{equ}-rich compositions. Further work is required to precisely determine solubility limits especially for Ni_{equ}-elements in chemically complex HE-SMAs.

3.5. Global (average) and local (individual constituents) chemical compositions

Fig. 7 provides an overview of relevant chemical compositions measured by EDX for alloys SenΔx-10 (average composition and constituents I, III, IV and V) and SenΔx1 (constituent II). Fig. 7a documents the average alloy composition of SenΔx-10. The compositions of its individual microstructural constituents obtained by EDX point analysis are shown in Fig. 7 b, d, e and f. The chemical composition of microstructural constituent II, which only formed in SenΔx1 is shown in Fig. 7c. Ni-equivalent elements are represented in blue tones, while Ti-equivalent elements are shown in different hues of green as indicated by the color-coding. Fig. 7a, confirms that

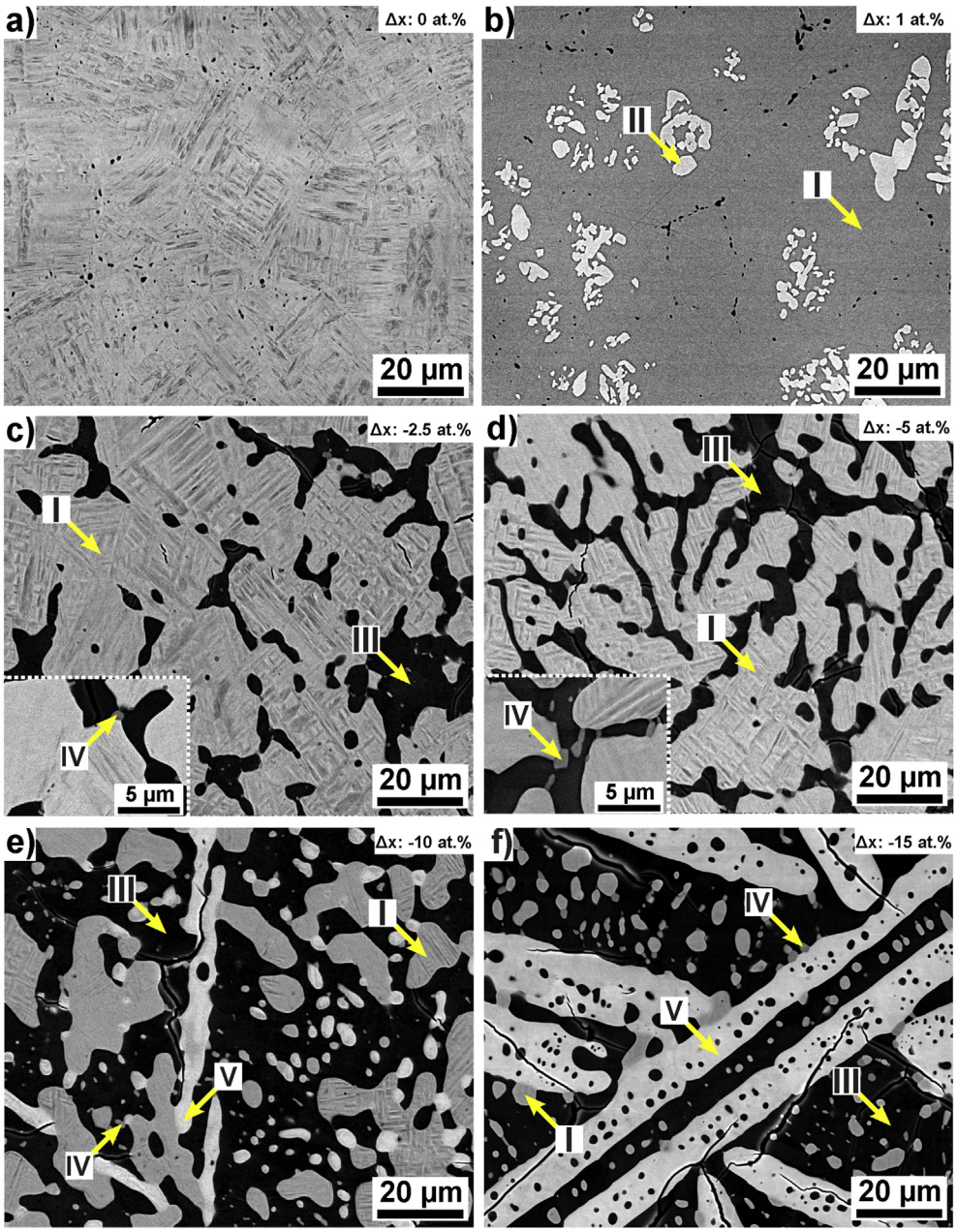

Fig. 4. SEM backscatter micrographs of Ni-Cu-Pd-Ti-Zr-Hf alloys with different compositions after homogenization annealing at 1173 K for 100 h. See main text for details on the definition of the five microstructural constituents labeled I, II, III, IV and V. (a) Stoichiometric composition. (b) $\Delta x = 1$ at.%. (c) $\Delta x = -2.5$ at.%. (d) $\Delta x = -5$ at.%. (e) $\Delta x = -10$ at.%. (f) $\Delta x = -15$ at.%.

the average composition of the ingot is close to the target alloy composition, Table 1. The composition of the microstructural constituent I in Fig. 7b significantly deviates from the target alloy composition. Most importantly, it has a significantly lower Ti-concentration, and there are higher levels of Ni, Cu and Pd. However, when the concentrations of Ni, Cu and Pd (Ni-equivalent elements) are summed up, the resulting $x_{Ni\text{-}equ}$ concentration is very close to 50 at.%. This is in line with what one would expect for binary Ni-Ti alloys [45], Fig. 1. This demonstrates that in spite of the relatively large Δx-shift of −10 at.%, the microstructural constituent I maintains quasi-stoichiometry. Microstructural constituent II, which is only observed in the over quasi-stoichiometric HE-SMAs in Fig. 4b, contains relatively large amounts of Cu, Fig. 7c. The compositions of the other constituents III, IV and V are shown in Fig. 7d−f, they all contain between 32 and 36 at.% of Ni-equivalent elements. However, these phases differ with respect to the amounts of individual elements, Fig. 7 d-f. Thus, the dark appearing phase (constituent III, Fig. 4e/7d) has a higher Ti-concentration. Constituent IV, on the other hand, shows a low Cu level, Figs. 4e and 7e. The bright appearing constituent V, Fig. 4e/7f, exhibits a high Hf-concentration in combination with a relatively low Ni-content. Fig. 8 shows how the compositions of the constituents of SenΔx-10 depend on the deviations from ideal stoichiometry. The data compiled in Fig. 8 document that all constituents change their composition when Δx is altered. For the sake of brevity not all individual trends will be described in detail. However, it is important to highlight three aspects, which are associated with more negative Δx values: First, the Ti-concentration in constituent I decreases, while the Hf-content

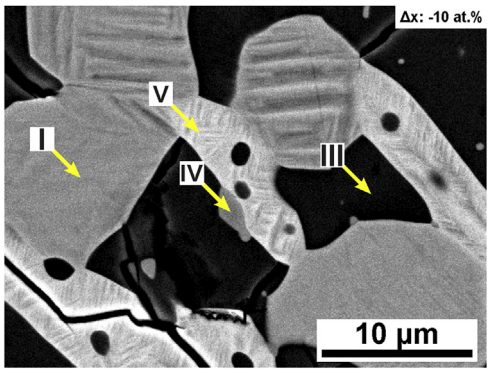

Fig. 5. SEM backscatter micrograph of the senary alloy SenΔx-10. Microstructural constituent V exhibits pronounced plate-/needle-like martensite features.

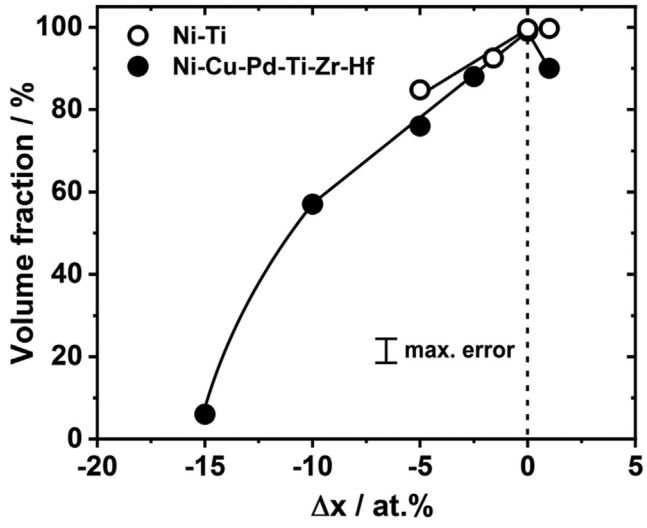

Fig. 6. Dependence of volume fraction of microstructural constituent I (B2/B19′) on chemical compositions expressed in terms of the deviation from stoichiometry/quasi stoichiometry, Δx.

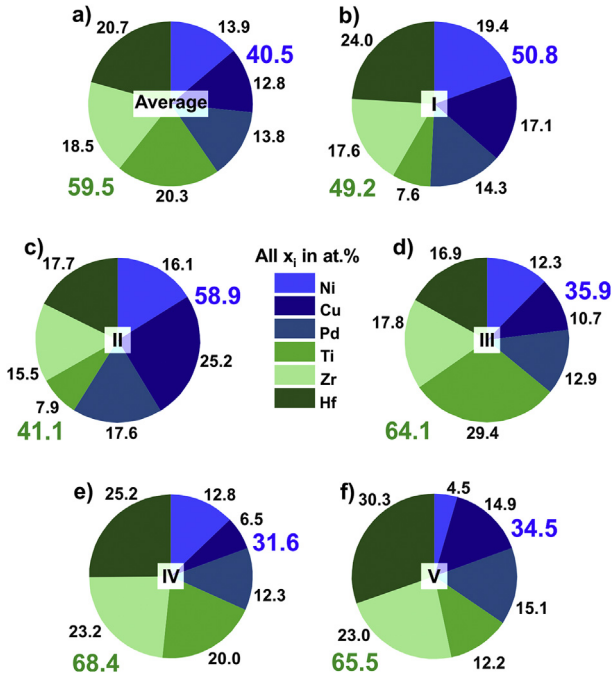

Fig. 7. Global (average) and local chemical compositions (individual microstructural constituents) measured for alloys SenΔx-10 (average composition and constituents I, III, IV and V) and SenΔx1 (constituent II). All compositions in at.%. Elements identified by color coding. Blue tones: Ni-equivalent elements. Green tones: Ti-equivalent elements. (a) Average composition of SenΔx-10. Microstructural constituents: (b) I in SenΔx-10. (c) II in SenΔx1. (d, e, f) III, IV and V in SenΔx-10 as indicated.

increases, Fig. 8a. Second, relatively slight changes are observed for constituents III and V in Fig. 8b and d. Finally, constituent IV shows the strongest compositional changes, Fig. 8c.

3.6. Identification of phases in the TEM

Fig. 9a shows a FIB lamella of alloy SenΔx-10, which was prepared from a region that contained the three microstructural constituents I, III and V. At the three positions, TEM images and electron diffraction patterns were recorded. Fig. 9b shows a TEM bright field image taken from the location marked as I in Fig. 9a. The microstructure shows typical martensitic features (martensite variants and/or twins). A corresponding selected area electron diffraction (SAED) pattern, taken from the region highlighted with a white circle in Fig. 9b, is presented in Fig. 9c. The diffraction pattern can be rationalized on the basis of the B19′ crystal structure as reported for the Cu–Zr system [62]. It has a monoclinic angle of $\beta = 104.3°$ (indicated in Fig. 9c), which is larger than that observed in binary Ni-Ti ($\beta = 97.78°$ [63]). The two white arrows point to two diffraction spots, one with a high and the other with a low intensity. These are twin related diffraction spots, which reveal the presence of a [001]-compound twin. Fig. 10a shows a TEM bright field image of constituent III (as marked in Fig. 9a), with superimposed bending contours. The region highlighted with a white circle was probed by SAED. The three SAED patterns in Fig. 10b, c and d were taken at different tilt positions. In the SAED pattern shown in Fig. 10b, the electron beam is parallel to the [111] zone of the cubic Zr_2Cu phase [64]. The presence of this phase can be confirmed by diffraction results obtained for other tilt positions (Fig. 10c: [552] zone of Zr_2Cu; Fig. 10d: [441] zone of Zr_2Cu). Fig. 11 summarizes the TEM results for constituent V in Fig. 9a. Fig. 11a shows the TEM bright field image of constituent V. Fig. 11b shows a SAED pattern from the encircled region in Fig. 11a, where the electron beam is parallel to [010] of the tetragonal Zr_2Cu crystal lattice [65,66]. This is supported by the SAED patterns shown in Fig. 11c and d, where the specimen was tilted into a position where the electron beam is parallel to [110] and [331], respectively. Thus the three constituents I, III and V in SenΔx-10 can be identified based on phases that characterize the binary Cu–Zr system [62,64,67]. No effort was made to identify the microstructural constituents II and IV. Constituent II only is observed in the Ni_{equ}-rich HE-SMA, which is not considered further in the present study. Constituent IV was also not investigated further because it only occurs in negligible small quantities in the ΔSen-10 alloy.

3.7. Thermal transformation behavior of senary alloys

DSC charts which document the phase transformation behavior of all senary alloys are presented in Fig. 12. Fig. 12 shows that the alloy compositions significantly affect transformation behavior. The HE-SMA alloy with a Δx value of 1 has a martensite start temperature M_S of around 230 K. This temperature increases when the Δx

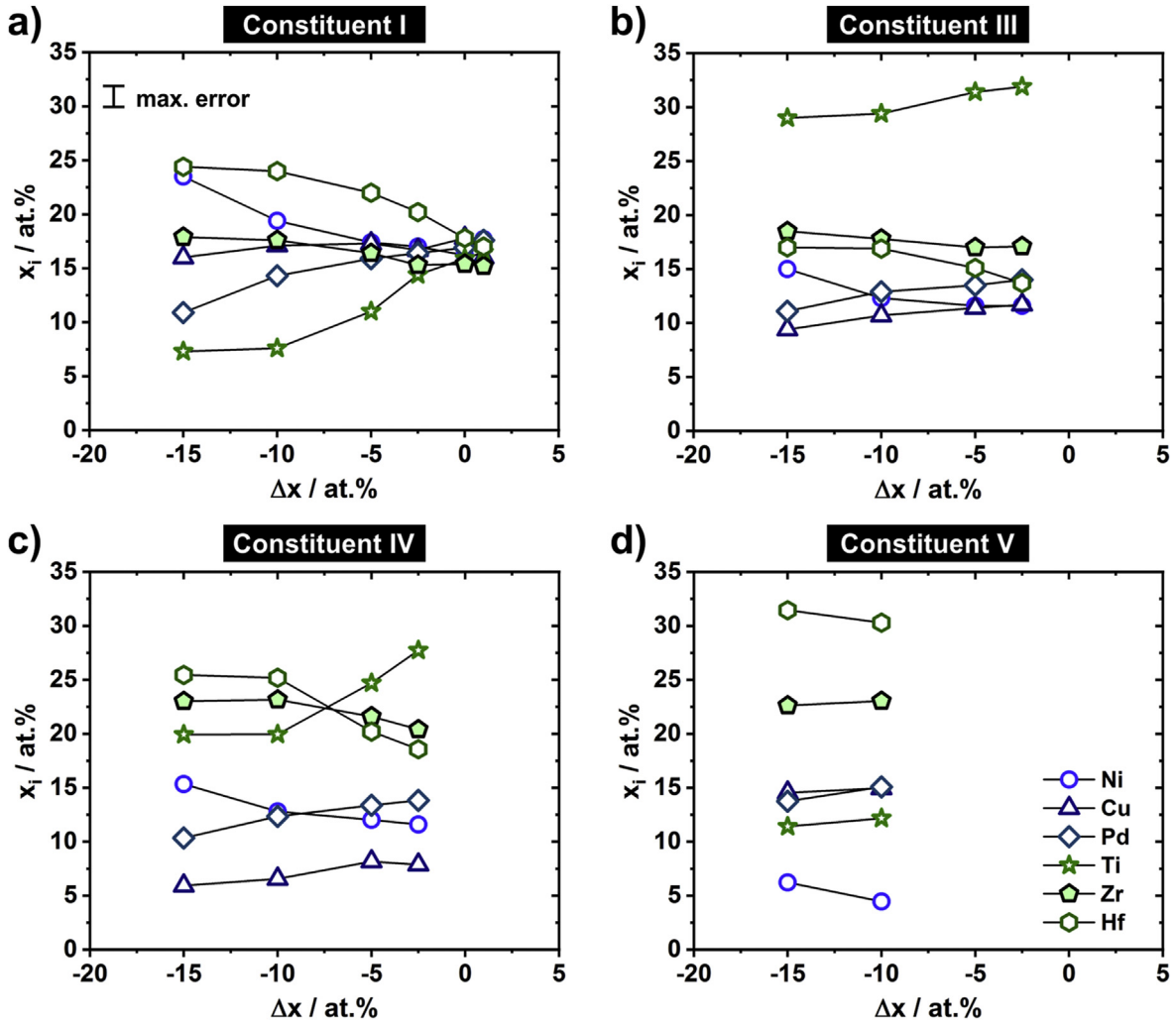

Fig. 8. Dependence of phase compositions on deviation from stoichiometric composition. (a) Constituent I, (b) constituent III, (c) constituent IV and (d) constituent V.

value shifts in the negative direction. For the SenΔx-10 HE-SMA, a M_S temperature of around 571 K was determined, whereas no transformations could be detected for the SenΔx-15 alloy (DSC data not shown). It is assumed that the volume fraction of the microstructural constituent that can undergo the martensitic transformation was probably too small to yield a detectable thermal effect (see Figs. 4 and 6). An interesting behavior was observed for the HE-SMA SenΔx-10, Fig. 12. The thermal hysteresis width ΔT_H of this material exceeds 250 K. Table 3 compiles all basic parameters which characterize forward (martensite start, peak and finish temperatures M_S, M_P and M_F; latent heat ΔH_{AM}) and the reverse transformation (austenite start, peak and finish temperature, A_S, A_P and A_F; latent heat ΔH_{MA}). In addition to the directly measured latent heats, Table 3 provides normalized latent heat data, ΔH_{AM}^{norm} and ΔH_{MA}^{norm} which were obtained by normalizing the ΔH_{MA} and ΔH_{MA} values by the volume fraction of microstructural constituent I (normalization data from Fig. 6). These normalized ΔH_{AM}^{norm} and ΔH_{MA}^{norm} values represent the latent heats, which rationalize the B2↔B19′ transformation.

4. Discussion

4.1. Thermodynamic aspects

The original HEA concept assumes that the high configurational entropy, resulting from a large number of equiatomic principal alloy elements, stabilizes single phase systems [22–26]. This stability is governed by the thermodynamic driving force ΔG_{mix}, which depends on the enthalpy of mixing ΔH_{mix} and the configurational entropy ΔS_{mix}:

$$\Delta G_{mix} = \Delta H_{mix} - T\Delta S_{mix}. \quad (1)$$

Interactions between metallic elements lead to the formation of intermetallic phases. This can be expressed by the driving force ΔG_{IM},

$$\Delta G_{IM} = \Delta H_{IM} - T\Delta S_{IM}, \quad (2)$$

where ΔH_{IM} and ΔS_{IM} represent the enthalpy and entropy terms associated with the formation of an intermetallic phase. The two enthalpy terms, ΔH_{mix} and ΔH_{IM}, depend on the energetic interactions between the different metallic elements. The entropy terms, ΔS_{mix} and ΔS_{IM}, on the other hand, are related to the probabilities of the arrangements of atoms. In an ideal HEA, ΔG_{mix} is

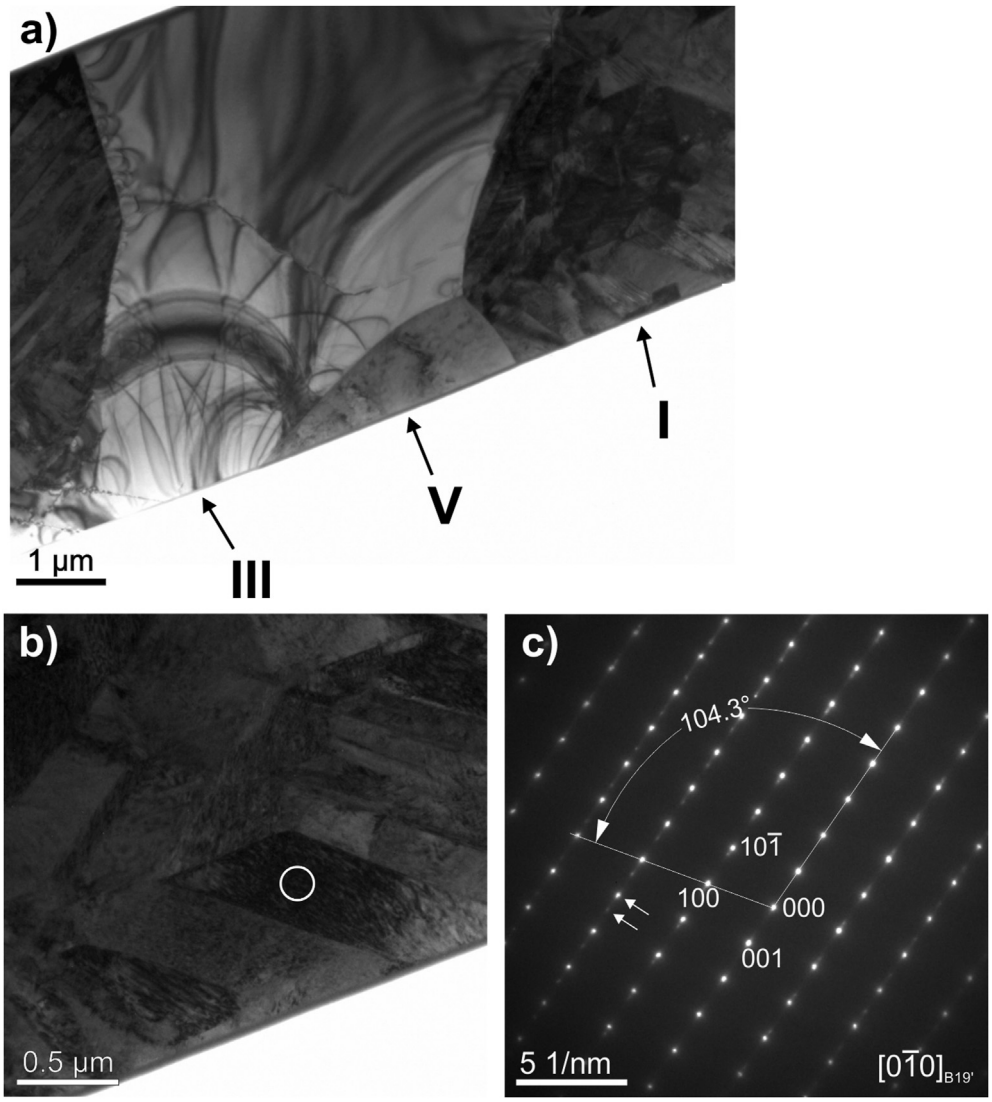

Fig. 9. TEM analysis of different phases. (a) TEM bright field image of a FIB lamella at lower magnification showing constituent I, III and V. (b) TEM bright field image of constituent I at higher magnification. (c) Selected area electron diffraction pattern from the encircled region in (b) in [0−10]-zone direction of the B19′-phase. The monoclinic angle of $\beta = 104.3°$ is marked and the two white arrows indicate the presence of a [001]-compound twin.

more negative than ΔG_{IM} [23–26,68]. This is promoted at higher temperatures, where the entropy term (product of T and ΔS_{mix}) increases. Maximum values for ΔS_{mix} are obtained for equimolar compositions, and they increase with an increasing number N of alloy components, $\Delta S_{mix} = R \cdot \ln(N)$, [23,30]. However, a high number of alloy components does not automatically establish a single-phase solid solution and it was documented that secondary phases form when HEAs are exposed to appropriate aging treatments [69,70], which do not too strongly promote mixing (T not too high) while not suppressing the kinetic processes required for phase nucleation and growth (T not too low).

One could have expected that the B2 phase (constituent I) in Ni-Cu-Pd-Ti-Zr-Hf HE-SMAs tolerates a larger degree of off-stoichiometry as compared to binary NiTi. The B2 phase with its equimolar composition actually represents an ideal candidate to obtain a stability boost by adding a larger number of additional elements. However, it was not possible to detect an effect of off-stoichiometry for the microstructural component I in isolation, because the formation of other phases could not be avoided, Figs. 3, 4 and 6. Moreover, the chemical stability range of austenite, and thus its solubility for other elements in HE-SMAs seems to be even lower than in binary NiTi, Fig. 6. This indicates that the thermodynamic driving force ΔG_{IM} outperforms ΔG_{mix}, Equations (1) and (2). Three thermodynamic/atomistic aspects account for this behavior: First, deviations from ideal stoichiometric compositions of intermetallic compounds often result in the formation of additional phases [71]. This is a general feature of many intermetallic systems and it especially holds for the B2 phase in Ni-Ti [42]. Compositional shifts towards higher Ti or Ni concentrations require the formation of anti-site defects [42]. The presence of these defects results in significantly higher enthalpies of formation for Ti-rich compositions, opposite to what is observed for systems with small amounts of excess Ni [42]. This explains why the B2 phase in Ni-Ti alloys has a certain solubility for excess Ni but not for additional Ti atoms. The reduced solubility for Ni-equivalent atoms in Ni-Cu-Pd-Ti-Zr-Hf alloys (see data for SenΔx1 in Fig. 6) can be related to a destabilization of the B2 phase, opposite to what is known for binary Ni-Ti. However, this behavior may also be caused by the formation of the Cu-rich phase II, Figs. 4b and 7c. The formation of this phase results in a stronger energy reduction of the total system as compared to the

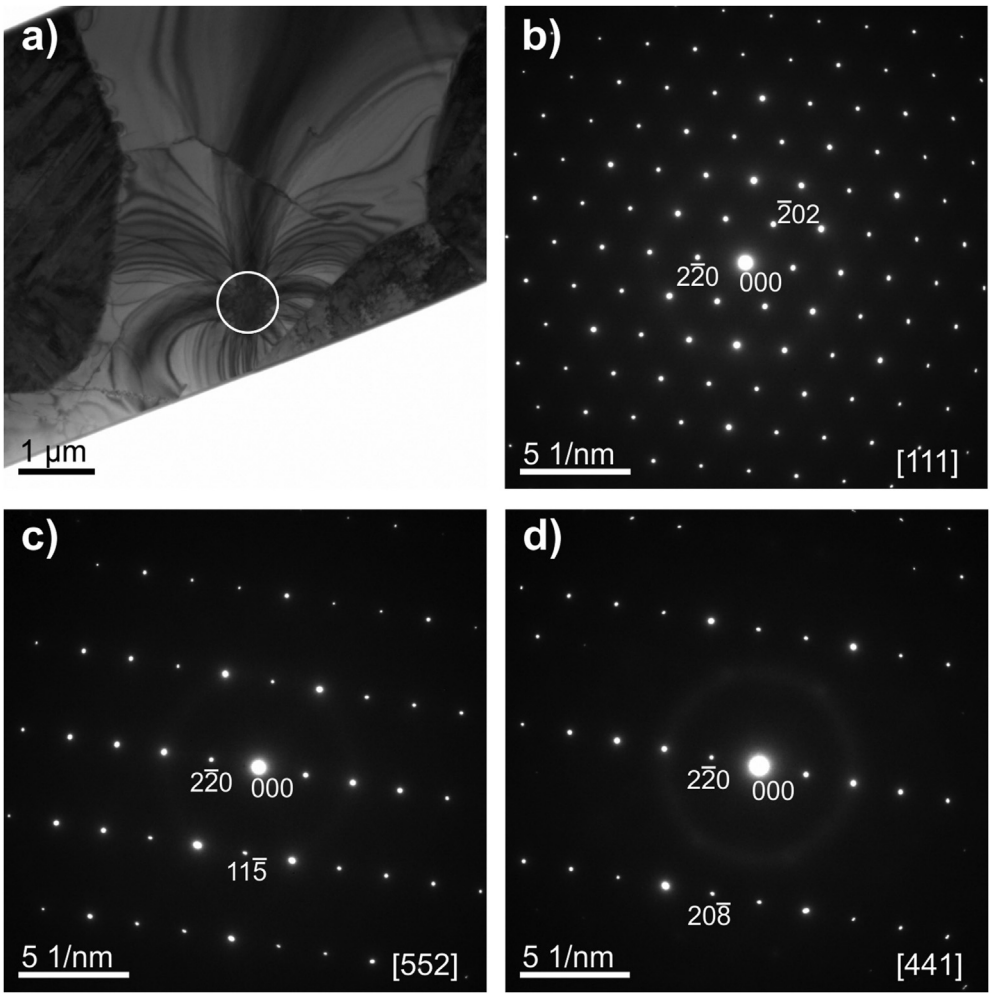

Fig. 10. TEM analysis of constituent III. (a) TEM bright field image. (b) Selected area electron diffraction pattern in [111]-zone direction of cubic Zr_2Cu type phase (Ti_2Ni prototype crystal structure) obtained from the encircled region in (a). (c) and (d) diffraction patterns in [552] and [441]-zone direction, respectively, obtained after tilting around the (2−20) plane.

formation of an over-stoichiometric B2 phase. Second, the different components in HE-SMAs are associated with large enthalpies of mixing [72,73], which indicates strong chemical interactions between the alloy elements. Therefore, the formation of ordered intermetallic compounds is generally preferred over the formation of solid solutions. Third, the ordering of crystal structures in HE-SMAs reduces configurational entropies [21], which translates into lower driving forces for the formation of ideal solid solutions.

4.2. Microstructures of off-stoichiometric HE-SMAs

The microstructures of HE-SMAs are significantly affected by the degree of over or under quasi-stoichiometry, Figs. 3, 4 and 6. They show a reduced solubility for excess Ni- or Ti-equivalent elements, Fig. 6. HE-SMAs with negative deviations from quasi-stoichiometry ($\Delta x < 0$) are characterized by the presence of several microstructural constituents that exist in parallel to constituent I, which can undergo the martensite ↔ austenite forward and reverse transformations, e.g. Fig. 4. Reducing the concentration of Ni-equivalent elements results in a decrease of the volume fraction of the microstructural constituent I and an increase of the fractions of the other microstructural constituents, Figs. 3, 4 and 6. This is analogous to what is known for the binary system Ni-Ti [45] which only contains two microstructural constituents, B2 austenite or B19' martensite and Ti_2Ni, Figs. 1 and 2. The different microstructural constituents in Fig. 4 and their chemical compositions (Figs. 7 and 8) can be interpreted based on a scenario, where all elements are assigned to two groups, which comprise all Ni- and Ti-equivalent atoms. Fig. 13 shows how the Ni-equivalent concentrations of the different phases depend on the degree of off quasi-stoichiometry of the entire alloy. Most importantly, the concentration of all Ni-equivalent elements, $x_{Ni\text{-}equ}$, of the microstructural constituent I (austenite/martensite) remains constant when Δx is varied. This also holds for the concentration of Ni, x_{Ni}, in binary Ni-Ti in the two-phase region B2/Ti_2Ni, Fig. 1. Additionally, the different phases (phases III-V in Figs. 4, 5 and 7) have $x_{Ni\text{-}equ}$ concentrations that are relatively close to 33 at.%, which again is similar to the situation in binary Ni-Ti, where Ti_2Ni forms with a Ni-concentration of 33 at.% [45]. However, only phase III, Fig. 4 c-f and 10, has a cubic type Zr_2Cu crystal structure (this could be observed after ball-milling) [64], which is equivalent to that of Ti_2Ni in binary Ni-Ti [45,74]. The structure of phase V corresponds to tetragonal Zr_2Cu [65], Fig. 11.

In a first step, one is tempted to conclude that these constitutional analogies between HE-SMAs and Ni-Ti were inherited from the binary reference system, Fig. 1. However, this would neglect possible contributions from other binary sub-systems. The six alloy elements in the present HE-SMAs form 15 binary sub-systems (Ni-

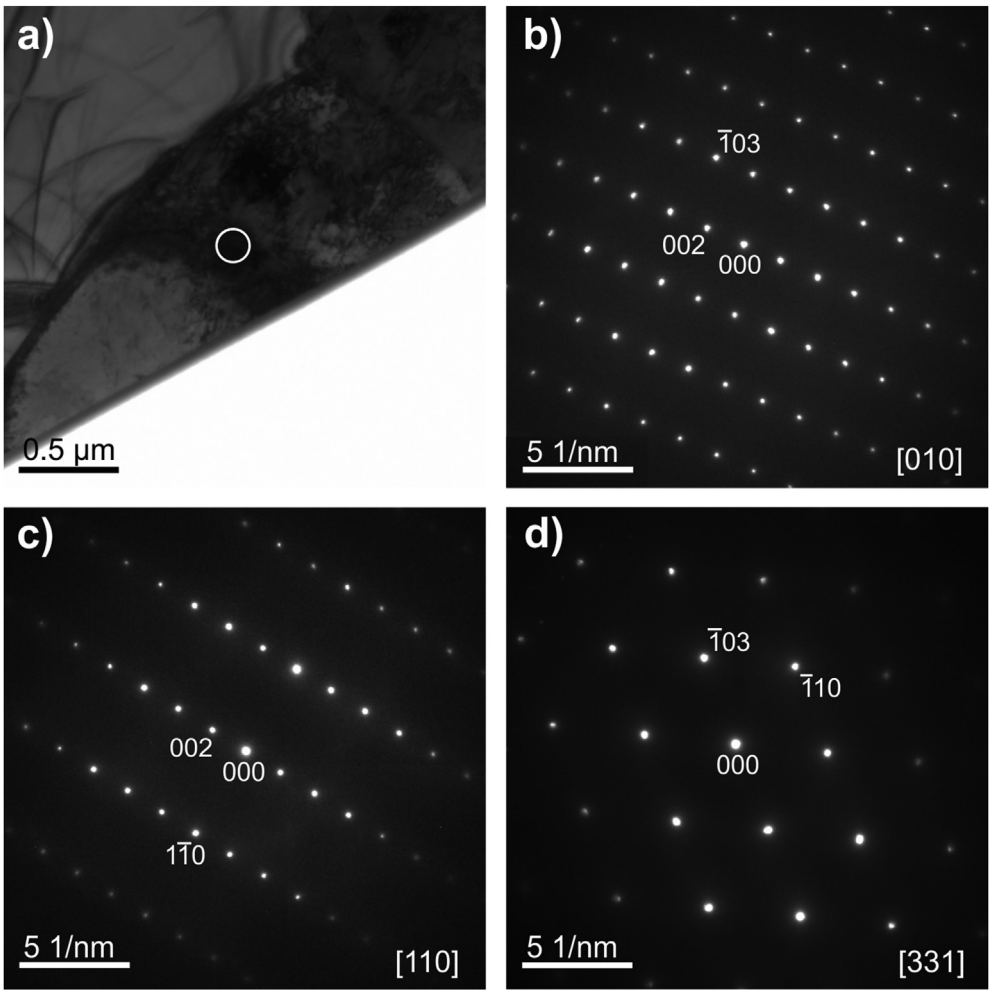

Fig. 11. Crystallographic analysis of constituent V. (a) TEM bright field image. (b) Selected area electron diffraction pattern in [010]-zone direction of tetragonal Zr_2Cu type phase (Si_2Mo prototype crystal structure) from the encircled region in (a). (c) and (d) diffraction patterns in [110] and [331]-zone direction, obtained after tilting around the (002)-plane and (−103)-plane, respectively.

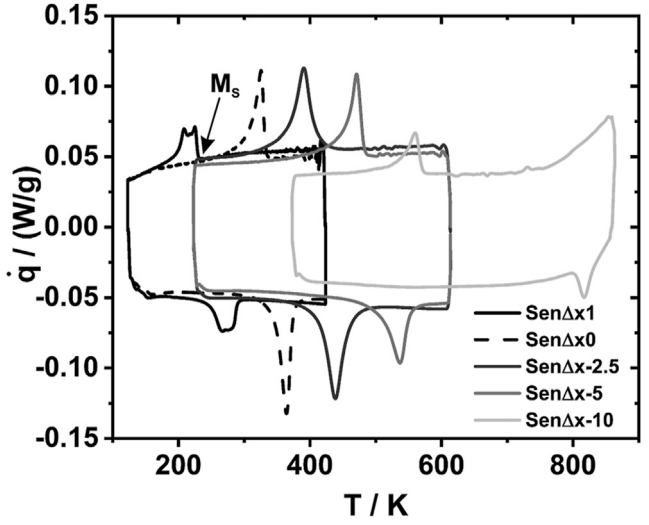

Fig. 12. DSC charts for senary Ni-Cu-Pd-Ti-Zr-Hf HE-SMA alloys with different compositions. One martensite start temperature M_S is exemplarily indicated for the SenΔx1 alloy.

Cu, Ni-Pd, Ni-Ti, Ni-Zr, etc.). One can reduce this number to 9, by only focusing on alloys which consist of one Ni-equivalent (Ni, Cu and Pd), and one Ti-equivalent (Ti, Zr and Hf) element. A closer look at thermodynamic and crystallographic literature data [28,45,62,65,67,74–89] shows that a number of similar features exist in these systems. Table 4 lists binary sub-systems, which contain the B2 phase (Table 4a), martensite (Table 4b) and phases with a 1:2 stoichiometry (Table 4c). In fact, 6 out of 9 relevant sub-systems contain the B2 phase, Table 4a, and all of these systems are known to show martensitic transformations [28,45,62,67,77,78, 81,84–89], Table 4b. Furthermore, all 9 systems show phases with a stoichiometry corresponding to that of Ti_2Ni [28,45,67,74,76,77, 80,82,84,87,89], Table 4c. However, certain dissimilarities also exist between these specific HE-SMA sub-systems and binary Ni-Ti. First, not all sub-systems exhibit solubilities for excess atoms in the B2 phase (systems with higher solubilities in the B2 phase, e.g. Ni-Hf [77,78] and Pd-Ti [84,85], are indicated in dark grey in Table 4a. Second, not all compositions show the same type of martensite [28,62,78,81,85,86,88], Table 4b. Some show B19′ martensite while others form B19 or B33 martensite instead. The system Ni-Zr represents a special case where B33 is supposed to form directly during solidification [76]. Concerning the phases with 1:2 stoichiometry, one has to note that various phases, which originate from three different crystal structure prototypes, exist in different

Table 3
Senary alloys: Phase transformation temperatures and latent heats ΔH_{AM} and ΔH_{MA}. M_S/A_S, M_P/A_P and M_F/A_F represent martensite/austenite start, peak and finish temperatures, respectively. Normalized latent heats, ΔH_{AM}^{norm} and ΔH_{MA}^{norm}, account for the volume fraction of the microstructural constituent which can undergo the martensitic transformation (see Fig. 6). The thermal hysteresis width ΔT_H represents the temperature-interval between A_P and M_P.

Alloy	M_S (K)	M_P (K)	M_F (K)	A_S (K)	A_P (K)	A_F (K)	ΔH_{AM} (J/g)	ΔH_{MA} (J/g)	ΔH_{AM}^{norm} (J/g)	ΔH_{MA}^{norm} (J/g)	ΔT_H (K)
SenΔx1	229.8	224.9	196.4	249.0	267.3	290.1	4.1	−4.5	4.6	−5.0	42.4
SenΔx0	332.6	352.4	303.8	334.8	364.2	375.1	8.2	−9.4	8.3	−9.5	38.6
SenΔx-2.5	382.7	369.4	346.0	401.1	420.1	429.0	8.0	−9.4	9.1	−10.7	50.7
SenΔx-5	482.4	471.2	455.5	508.5	536.0	550.9	9.1	−8.2	12.0	−10.8	64.8
SenΔx-10	570.7	559.9	535.8	804.0	816.8	829.9	5.5	−2.9	9.6	−5.1	256.9

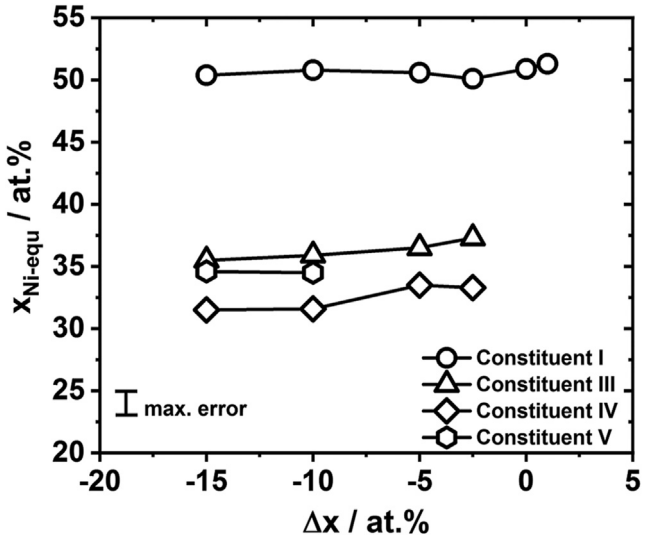

Fig. 13. Dependence of the Ni-equivalent concentration of the microstructural constituents that are observed in Ni-Cu-Pd-Ti-Zr-Hf HE-SMAs with different compositions.

subsystems, Table 4c. In some cases, these phases form as primary phases as indicated by bold letters.

It seems reasonable to assume that some of the crystallographic and chemical features of the present HE-SMAs discussed above were inherited from the different binary sub-systems. Thus, senary Ni-Cu-Pd-Ti-Zr-Hf HE-SMAs show (1) the B2 phase [21], (2) B19′ martensite (Fig. 9) and (3) phases with 1:2 stoichiometries (Figs. 4, 7, 10, 11 and 13), Table 4. The microstructural information presented in Fig. 4 allows concluding that also reaction paths and certain microstructural characteristics in HE-SMAs were inherited from the different sub-systems. For example, phase III in Fig. 4 has a crystal structure that is equivalent to Ti_2Ni, Fig. 11, and it is located in intercellular constituent I (B2/B19′) regions, Fig. 4c and d. In binary Ni-Ti alloys, this phase forms by a peritectic reaction [45] which yields a similar microstructure, Fig. 2c. Therefore, it is suggested that a similar reaction governs the formation of the cubic Ti-rich phase III in Ni-Cu-Pd-Ti-Zr-Hf HE-SMAs. In contrast, the tetragonal phase V, which is rich in Zr and Hf, forms long elongated particles (Fig. 4e and f, 7 and 11) and probably evolved as a primary phase during solidification. This thermodynamic feature apparently has been passed on from the sub-systems Cu-Zr [67], Cu-Hf [82] and Pd−Zr [87], Table 4c. With this in mind, it is worth to mention that the equivalent Hf_2Cu phase (see Fig. 8a in Ref. [90] and Fig. 3 in Ref. [91]) shows almost the same morphology as observed for the Hf-rich phase V in Fig. 4e and f. In summary, the microstructures of senary Ni-Cu-Pd-Ti-Zr-Hf HE-SMAs contain basic features which can be found in various binary sub-systems [28,45,62,65,67,74–89]. It cannot be ruled out that other effects caused by chemical interactions between more than two elements also play a role. However, the microstructural results of the present study suggest that these effects are not of primary importance. Further work is required to clarify this point.

4.3. Martensitic transformations in off quasi-stoichiometric HE-SMAs

Fig. 12 shows that deviations from the ideal (quasi-stoichiometric) alloy composition of HE-SMAs have a strong effect on phase transition temperatures. Fig. 14 shows how M_S temperatures of binary Ni-Ti and of senary HE-SMAs depend on the *nominal* (entire) alloy composition. In both alloy systems, Ti/Ti_{equ}-rich compositions

Table 4
Brief overview of austenite, martensite and Ti_2Ni type phases in binary HE-SMA sub-systems [28,45,62,65,67,74–89]. Grey fields indicate that there is solubility for excess atoms. Bold letters indicate that the phases can solidify as primary phase. Ti_2Ni has a cubic structure (Fd-3m), while $CuAl_2$ (I4/mcm) and $MoSi_2$ (I4/mmm) possess a tetragonal crystal structure. (a) B2. (b) Martensite. (c) Compound phases.

a) B2 phase

	Ti	Zr	Hf
Ni	✓	-	✓
Cu	-	✓	-
Pd	✓	✓	✓

b) Martensite

	Ti	Zr	Hf
Ni	B19'	**(B33)**	B33
Cu	-	B19'/ B33	-
Pd	B19	B33	B33

c) Phase prototypes with 1:2 stoichiometry

	Ti	Zr	Hf
Ni	Ti_2Ni	**$CuAl_2$**	$CuAl_2$
Cu	$MoSi_2$	**$MoSi_2$**, Ti_2Ni	**$MoSi_2$**
Pd	$MoSi_2$	**$MoSi_2$**	$MoSi_2$

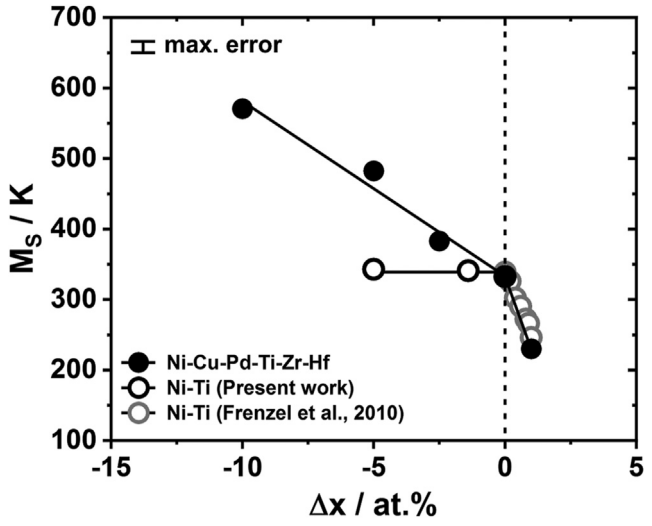

Fig. 14. Effect of *nominal/entire* alloy compositions (expressed through Δx shifts) on martensite start temperatures for binary and senary alloy systems.

consist of multiple phases. In the case of binary Ni-Ti, we find B2/B19′ and Ti_2Ni phases, while B2/B19′ and phases with a stoichiometry comparable to Ti_2Ni are present in the senary alloys, Figs. 2, 4 and 7. In Fig. 14, M_S data from previous work [43] with the results obtained in the present study are compared. The data confirm that significant differences exist between conventional binary and high entropy SMAs when nominal alloy compositions are altered. HE-SMAs show higher transformation temperatures for under quasi-stoichiometric compositions ($\Delta x < 0$). Most importantly, the compositional dependence of M_S in HE-SMAs is fundamentally different from that of binary Ni-Ti alloys [42,43]. While binary Ni-Ti SMAs show constant M_S temperatures for under-stoichiometric alloy compositions, a negative Δx-shift towards Ti_{equ}-rich alloy compositions (under quasi-stoichiometric alloy compositions) results in an increase of M_S. This finding is unexpected because this increase is observed in a compositional range where the chemistry of the microstructural constituent I (B2 or B19′) in terms of Ni-/Ti-equivalent concentrations hardly changes, Fig. 13. The trend documented in Fig. 14 cannot simply be rationalized based on Ni-equivalent concentrations of the entire alloys. In fact, M_S temperatures in Ti_{equ}-rich HE-SMAs seem to be governed by changes in the concentrations of *individual* alloy elements for constituent I, Fig. 8a. In contrast to the concentrations of Ni-equivalent elements, $x_{Ni\text{-}equ}$, the concentrations of individual alloy elements in constituent I are significantly affected, when Δx is altered, Fig. 8a. The compositional changes documented in Fig. 8a suggest that although different phases form, Fig. 4 c-f, the HE-SMA system still has a sufficiently high number of degrees of freedom to vary phase compositions. This is an important difference to binary Ni-Ti, Fig. 1, where Gibb's phase rule prohibits such changes [92].

An attempt to rationalize how the different elements in Ni-Cu-Pd-Ti-Zr-Hf HE-SMAs affect phase transformation temperatures was made in our previous study [21]. It was found that increasing Hf and Zr levels result in an increase of M_S temperatures. This is in line with observations reported in literature for classical ternary high temperature SMAs, e.g. Refs. [7,27,42,93,94]. However, the additions of Cu and (surprisingly) Pd resulted in lower M_S values [21]. The previous findings allow to rationalize the trends observed in the present study, Figs. 12 and 14. A compositional shift towards higher Ti_{equ}-rich compositions (more negative Δx values) results in higher Hf and lower Pd concentrations of constituent I, Fig. 8a. This therefore could promote higher transformation temperatures, Figs. 12 and 14, although the corresponding compositions show higher Ni-concentrations which - for binary Ni-Ti SMAs - would result in the opposite effect [43]. Further work is required to better understand the effects of individual element concentrations.

In order to validate whether concentration changes in off-stoichiometric HE-SMAs can affect transformation behavior, valence electron concentrations were calculated for the microstructural constituent I (B2/B19′) from the EDX data shown in Fig. 8a. The resulting $M_S(c_V)$ data are plotted in Fig. 15 together with data points from the literature [15,21,42,43,93,94]. Note that Fig. 15 incorporates the literature data collected and published by Zarinejad and Liu (Z&L) [93,94]. They have shown that M_S temperatures for a large number of Ni-Ti-based SMAs depend on valence electron concentrations c_V and that decreasing c_V values result in an increase of M_S. In a previous publication, it was discussed that this only holds when one takes a broad view and accepts large deviations [42]. The data do not fall on one master curve; instead they form a broad scatter band, which is highlighted in light grey in Fig. 15. For example, the strong compositional dependence of binary Ni-Ti alloys (high precision data sets [42,43]) cannot be rationalized by a c_V approach. While these high precision binary Ni-Ti data still fall in the Z&L scatter band, the senary HE-SMA data from the present paper (full circles in Fig. 15; c_V values derived from compositions of constituent I, Fig. 8a) do not. In fact, they show M_S values that are much lower than even the lowest data in the Z&L scatter band. Possible reasons for this behavior have been discussed previously [21]. The present data clearly suggest that changing the concentrations of individual alloy elements in constituent I related to negative Δx-shifts results in a small decrease of c_V and a simultaneous steep increase of M_S temperatures. The concentrations of individual alloy elements affect valence electron concentrations and M_S temperatures much stronger than one would expect. The importance and possible contributions of other factors have been discussed in previous studies [21,42] and may also play a role for the behavior observed in Figs. 12, 14 and 15.

The present study also revealed two additional unexpected findings, namely the martensite-like patterns observed in the Hf-rich phase V, Fig. 5, and the presence of a large hysteresis width in the SenΔx-10 HE-SMA, Fig. 12. The large hysteresis width is among the largest widths ever reported in scientific literature on SMAs, e.g. Ref. [42]. The reasons for this large hysteresis width are

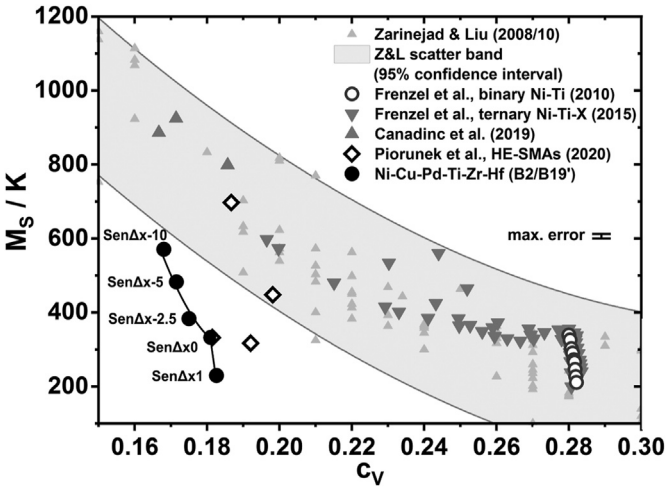

Fig. 15. Correlation between valence electron concentration c_V of the B2/B19′ phase (corresponding to constituent I in Fig. 4, which exhibits martensitic transformations) and martensite start temperature (literature references: [15,21,42,43,93,94]).

not clear at present. It is therefore interesting to investigate whether this is related to the crystallography of martensite and austenite, as it has been discussed in literature on various occasions, e.g. Refs. [95–97], or to other microstructural effects. Further work is required to rationalize this observation. As an outlook, it is required to study cyclic stability of martensitic transformation in the different HE-SMAs. It is interesting to investigate whether solid-solution strengthening effects affect functional fatigue [98], and whether the presence of larger amounts of secondary phases (which may be expected to deteriorate shape memory performance) affect functional behavior.

4.4. New paths for SMA developments

The findings obtained in the present study point into directions for the development of future shape memory alloys. The data presented in Figs. 8a and 12-15 suggest that it is possible to vary concentrations of *individual* elements in larger compositional ranges to control phase transformation temperatures. However, there is one restriction: Alloy compositions have to be chosen such that the ratio between the concentrations of Ni- and Ti-equivalent elements remains equimolar. This is a requirement to prevent a chemical destabilization of the B2 phase. Note that a large number of conventional NiTi-based SMAs studied in the literature actually obey this rule. This also holds for various ternary and quaternary alloys [42,99], for high temperature SMAs [27,42,100], for recent "ultra-high temperature multi-component" SMAs proposed by Canadinc et al. [15], and also for the Firstov HE-SMAs [11–13]. However, many previous studies focus on alloy compositions which were based on or inspired by stoichiometric NiTi. Therefore, Ni and Ti concentrations are dominating in these alloys (e.g. $Ni_{45}Cu_5Ti_{50}$ [37], $Ti_{50.2}Ni_{34.4}Cu_{12.3}Pd_{3.1}$ [38], $Ti_{50.8}$ $Ni_{34.2}$ $Cu_{12.5}Co_{2.5}$ [101]). In many cases, only one element of the base-material was partially substituted. The results of the present study, Figs. 1, 7 and 12–14, suggest that it is possible to obtain martensitic transformations in multi-component alloys with compositions far away from binary NiTi as long as quasi-stoichiometry is maintained. Therefore, it is well worth to explore solubility limits when concentrations of individual elements are significantly altered, and to systemically screen new compositional regimes. It should be noted that the rule suggested above is not restricted to SMAs with a large number of alloy components. Most likely, it is also valid for HE-SMA subsystems with lower chemical complexity. Against this background, one may again consider the high numbers of binary HE-SMA subsystems in Table 4b, where martensitic transformations have been observed [28,45,62,67,77,78,81,84–89]. There is a need to figure out how large the compositional multi-component space is in which martensitic transformations and shape memory effects can be exploited. Further work is required to explore this SMA development concept.

5. Summary and conclusions

The present study investigates how microstructures and phase transformation behavior in binary and chemically complex NiTi-based shape memory alloys (referred to as high entropy shape memory alloys, HE-SMAs) evolve when alloy compositions deviate from an ideal stoichiometry (binary NiTi) or quasi-stoichiometry (NiTi-derived HE-SMAs), where the concentrations of all Ni-equivalent and all Ti-equivalent alloy elements are 50 at.%. From the results obtained in the present study, the following conclusions can be drawn:

(1) Basic fundamental thermodynamic and microstructural features of chemically complex Ni-Cu-Pd-Ti-Zr-Hf HE-SMAs can be traced back to the constitutional properties of nine binary HE-SMA sub-systems which consist of the Ni-equivalent elements Ni, Cu and Pd (first element in binary sub-system) and Ti-equivalent elements Ti, Zr and Hf (second element in binary sub-system).
(2) In contrast to binary Ni-Ti SMAs, Ni-Cu-Pd-Ti-Zr-Hf HE-SMAs show a reduced solubility for excess Ni-equivalent elements. However, transformation temperatures can be altered by excess amounts of Ti-equivalent elements.
(3) Several phases form in HE-SMAs (Ti_{equ}-rich HE-SMAs) with higher concentrations of Ti-equivalent elements (negative deviation from ideal quasi-stoichiometry). These phases were identified as cubic Ti-rich Ti_2Ni and a tetragonal Zr/Hf-rich Si_2Mo-type phase.
(4) All Ti_{equ}-rich HE-SMAs considered in the present work show higher phase transformation temperatures as compared to binary Ni-Ti alloys, whereas a similar behavior was observed in both systems for Ni_{equ}-rich composition regimes. New results were presented which document how M_S temperatures of HE-SMAs depend on the off quasi-stoichiometry of the B2 phase. The M_S temperatures of the senary HE-SMAs investigated in the present work are significantly lower than one would expect from the Zarinejad and Liu scatter band. The observed trends could be qualitatively interpreted based on the effects of individual alloy elements.
(5) A senary HE-SMA, $Ni_{13.333}Cu_{13.333}Pd_{13.333}Ti_{20}Zr_{20}Hf_{20}$, was identified which shows an unusual large thermal hysteresis width, and new directions for the design of advanced HE-SMAs are proposed which merit to be explored in future research.

CRediT authorship contribution statement

D. Piorunek: Investigation, Visualization, Writing - original draft, Writing - review & editing. **O. Oluwabi:** Investigation, Visualization. **J. Frenzel:** Conceptualization, Methodology, Supervision, Project administration, Funding acquisition, Writing - original draft, Writing - review & editing. **A. Kostka:** Investigation. **H.J. Maier:** Writing - review & editing, Funding acquisition. **C. Somsen:** Investigation, Visualization, Writing - original draft, Writing - review & editing. **G. Eggeler:** Conceptualization, Resources, Funding acquisition, Writing - review & editing.

Declaration of competing interest

The authors declare that they have no known competing financial interests or personal relationships that could have appeared to influence the work reported in this paper.

Acknowledgements

This study was supported by the German Research Foundation (DFG) through the priority program SPP 2006 "Legierungen mit komplexer Zusammensetzung – Hochentropielegierungen (CCA – HEA)" [grant numbers 313773923, 388671975]. The infrastructural support by the Zentrum für Grenzflächendominierte Höchstleistungswerkstoffe (ZGH) is gratefully acknowledged.

References

[1] J. Mohd Jani, M. Leary, A. Subic, M.A. Gibson, A review of shape memory alloy research, applications and opportunities, Mater. Des. (1980–2015) 56 (2014) 1078–1113.
[2] J. Frenzel, G. Eggeler, E. Quandt, S. Seelecke, M. Kohl, High-performance elastocaloric materials for the engineering of bulk- and micro-cooling

devices, MRS Bull. 43 (2018) 280–284.
[3] C. Bechtold, C. Chluba, R.L. De Miranda, E. Quandt, High cyclic stability of the elastocaloric effect in sputtered TiNiCu shape memory films, Appl. Phys. Lett. 101 (2012), 091903.
[4] T. Birk, S. Biswas, J. Frenzel, G. Eggeler, Twinning-induced elasticity in NiTi shape memory alloys, Shape Mem. Superelasticity 2 (2016) 145–159.
[5] H. Funakubo, Shape Memory Alloys, Gordon and Breach, New York, 1987.
[6] S. Miyazaki, K. Otsuka, Development of shape memory alloys, ISIJ Int. 29 (1989) 353–377.
[7] H. Sehitoglu, L. Patriarca, Y. Wu, Shape memory strains and temperatures in the extreme, Curr. Opin. Solid State Mater. Sci. 21 (2017) 113–120.
[8] D.C. Lagoudas, Shape Memory Alloys: Modeling and Engineering Applications, Springer, New York, 2008.
[9] E. Hornbogen, Shape memory alloys, in: W.G.J. Bunk (Ed.), Advanced Structural and Functional Materials, Springer Verlag, Köln, 1991, pp. 133–164.
[10] K. Bhattacharya, Microstructure of Martensite: Why it Forms and How it Gives Rise to the Shape-Memory Effect, Oxford University Press, Oxford, 2004.
[11] G.S. Firstov, T.A. Kosorukova, Y.N. Koval, V.V. Odnosum, High entropy shape memory alloys, Mater. Today-Proc. 2 (2015) 499–503.
[12] G. Firstov, A. Timoshevski, T. Kosorukova, Y. Matviychuk, P. Verhovlyuk, Electronic and crystal structure of the high entropy TiZrHfCoNiCu intermetallics undergoing martensitic transformation, MATEC Web Conf 33 (2015), 06006.
[13] G.S. Firstov, T.A. Kosorukova, Y.N. Koval, P.A. Verhovlyuk, Directions for high-temperature shape memory alloys' improvement: straight way to high-entropy materials? Shape Mem. Superelasticity 1 (2015) 400–407.
[14] A. Pasko, V. Kojomytsev, P. Vermaut, F. Prima, R. Portier, P. Ochin, A. Sezoneriko, Crystallization of the amorphous phase and martensitic transformations in multicomponent (Ti,Hf,Zr) (Ni, Cu)-based alloys, J. Non-Cryst. Solids 353 (2007) 3062–3068.
[15] D. Canadinc, W. Trehern, J. Ma, I. Karaman, F.P. Sun, Z. Chaudhry, Ultra-high temperature multi-component shape memory alloys, Scripta Mater. 158 (2019) 83–87.
[16] C.H. Chen, Y.J. Chen, Shape memory characteristics of (TiZrHf)(50)Ni25C-o10Cu15 high entropy shape memory alloy, Scripta Mater. 162 (2019) 185–189.
[17] H.C. Lee, Y.J. Chen, C.H. Chen, Effect of solution treatment on the shape memory functions of $(TiZrHf)_{50}Ni_{25}Co_{10}Cu_{15}$ high entropy shape memory alloy, Entropy 21 (2019).
[18] S.H. Li, D.Y. Cong, X.M. Sun, Y. Zhang, Z. Chen, Z.H. Nie, R.G. Li, F.Q. Li, Y. Ren, Y.D. Wang, Wide-temperature-range perfect superelasticity and giant elastocaloric effect in a high entropy alloy, Mater. Res. Lett. 7 (2019) 482–489.
[19] J.I. Lee, K. Tsuchiya, W. Tasaki, H.S. Oh, T. Sawaguchi, H. Murakami, T. Hiroto, Y. Matsushita, E.S. Park, A strategy of designing high-entropy alloys with high-temperature shape memory effect, Sci. Rep. 9 (2019) 10.
[20] H. Matsuda, H. Sato, M. Shimojo, Y. Yamabe-Mitarai, Improvement of high-temperature shape-memory effect by multi-component alloying for TiPd alloys, Mater. Trans. 60 (2019) 2282–2291.
[21] D. Piorunek, J. Frenzel, N. Jöns, C. Somsen, G. Eggeler, Chemical complexity, microstructure and martensitic transformation in high entropy shape memory alloys, Intermetallics 122 (2020) 106792, https://doi.org/10.1016/j.intermet.2020.106792.
[22] B. Cantor, I.T.H. Chang, P. Knight, A.J.B. Vincent, Microstructural development in equiatomic multicomponent alloys, Mater. Sci. Eng. A-Struct. 375 (2004) 213–218.
[23] J.W. Yeh, S.K. Chen, S.J. Lin, J.Y. Gan, T.S. Chin, T.T. Shun, C.H. Tsau, S.Y. Chang, Nanostructured high-entropy alloys with multiple principal elements: novel alloy design concepts and outcomes, Adv. Eng. Mater. 6 (2004) 299–303.
[24] Y. Zhang, T.T. Zuo, Z. Tang, M.C. Gao, K.A. Dahmen, P.K. Liaw, Z.P. Lu, Microstructures and properties of high-entropy alloys, Prog. Mater. Sci. 61 (2014) 1–93.
[25] D.B. Miracle, O.N. Senkov, A critical review of high entropy alloys and related concepts, Acta Mater. 122 (2017) 448–511.
[26] E.P. George, D. Raabe, R.O. Ritchie, High-entropy alloys, Nat. Rev. Mater. 4 (2019) 515–534.
[27] J. Ma, I. Karaman, R.D. Noebe, High temperature shape memory alloys, Int. Mater. Rev. 55 (2010) 257–315.
[28] K. Otsuka, X. Ren, Physical metallurgy of Ti-Ni-based shape memory alloys, Prog. Mater. Sci. 50 (2005) 511–678.
[29] O.N. Senkov, G.B. Wilks, D.B. Miracle, C.P. Chuang, P.K. Liaw, Refractory high-entropy alloys, Intermetallics 18 (2010) 1758–1765.
[30] Z. Wu, H. Bei, G.M. Pharr, E.P. George, Temperature dependence of the mechanical properties of equiatomic solid solution alloys with face-centered cubic crystal structures, Acta Mater. 81 (2014) 428–441.
[31] T. Waitz, T. Antretter, F.D. Fischer, N.K. Simha, H.P. Karnthaler, Size effects on the martensitic phase transformation of NiTi nanograins, J. Mech. Phys. Solid. 55 (2007) 419–444.
[32] R. Delville, B. Malard, J. Pilch, P. Sittner, D. Schryvers, Transmission electron microscopy study of microstructural evolution in nanograined Ni-Ti microwires heat treated by electric pulse, Solid State Phenom. 172–174 (2011) 682–687.
[33] J. Burow, J. Frenzel, C. Somsen, E. Prokofiev, R. Valiev, G. Eggeler, Grain nucleation and growth in deformed niti shape memory alloys: an in situ TEM study, Shape Mem. Superelasticity 3 (2017) 347–360.
[34] K. Gall, H. Maier, Cyclic deformation mechanisms in precipitated NiTi shape memory alloys, Acta Mater. 50 (2002) 4643–4657.
[35] F. Yang, D.R. Coughlin, P.J. Phillips, L. Yang, A. Devaraj, L. Kovarik, R.D. Noebe, M.J. Mills, Structure analysis of a precipitate phase in an Ni-rich high-temperature NiTiHf shape memory alloy, Acta Mater. 61 (2013) 3335–3346.
[36] A. Evirgen, I. Karaman, R. Santamarta, J. Pons, R.D. Noebe, Microstructural characterization and shape memory characteristics of the Ni50.3Ti34.7Hf15 shape memory alloy, Acta Mater. 83 (2015) 48–60.
[37] C. Grossmann, J. Frenzel, V. Sampath, T. Depka, G. Eggeler, Elementary transformation and deformation processes and the cyclic stability of NiTi and NiTiCu shape memory spring actuators, Metall. Mater. Trans. 40 (2009) 2530–2544.
[38] R. Zarnetta, R. Takahashi, M.L. Young, A. Savan, Y. Furuya, S. Thienhaus, B. Maaß, M. Rahim, J. Frenzel, H. Brunken, Y.S. Chu, V. Srivastava, R.D. James, I. Takeuchi, G. Eggeler, A. Ludwig, Identification of quaternary shape memory alloys with near-zero thermal hysteresis and unprecedented functional stability, Adv. Funct. Mater. 20 (2010) 1917–1923.
[39] K.C. Atli, B.E. Franco, I. Karaman, D. Gaydosh, R.D. Noebe, Influence of crystallographic compatibility on residual strain of TiNi based shape memory alloys during thermo-mechanical cycling, Mater. Sci. Eng., A 574 (2013) 9–16.
[40] S. Jaeger, B. Maaß, J. Frenzel, M. Schmidt, S. Seelecke, O. Kastner, G. Eggeler, On the widths of the hysteresis of mechanically and thermally induced martensitic transformations in Ni-Ti based shape memory alloys, Int. J. Mater. Res. 106 (2015) 1029–1039.
[41] C. Chluba, W.W. Ge, R.L. de Miranda, J. Strobel, L. Kienle, E. Quandt, M. Wuttig, Ultralow-fatigue shape memory alloy films, Science 348 (2015) 1004–1007.
[42] J. Frenzel, A. Wieczorek, I. Opahle, B. Maaß, R. Drautz, G. Eggeler, On the effect of alloy composition on martensite start temperatures and latent heats in Ni-Ti-based shape memory alloys, Acta Mater. 90 (2015) 213–231.
[43] J. Frenzel, E.P. George, A. Dlouhy, C. Somsen, M.F.X. Wagner, G. Eggeler, Influence of Ni on martensitic phase transformations in NiTi shape memory alloys, Acta Mater. 58 (2010) 3444–3458.
[44] W. Tang, B. Sundman, R. Sandstrom, C. Qiu, New modelling of the B2 phase and its associated martensitic transformation in the Ti-Ni system, Acta Mater. 47 (1999) 3457–3468.
[45] J.L. Murray, Ni-Ti (Nickel-Titanium), in: T.B. Massalski, H. Okamato, P.R. Subramanian, L. Kacprzak (Eds.), Binary Alloy Phase Diagrams, ASM International, Materials Park, Ohio, 1990, pp. 2874–2876.
[46] G.F. Bastin, G.D. Rieck, Diffusion in the titanium-nickel system: I. occurrence and growth of the various intermetallic compounds, Metall. Trans. 5 (1974) 1817–1826.
[47] T. Duerig, A. Pelton, D. Stöckel, An overview of Nitinol medical applications, Mater. Sci. Eng., A 273–275 (1999) 149–160.
[48] T.W. Duerig, A.R. Pelton, An overview of superelastic Stent design, Mater. Sci. Forum 394–3 (2001) 1–8.
[49] M. Nishida, C.M. Wayman, T. Honma, Precipitation processes in near-equiatomic tini shape memory alloys, Metall. Trans. A 17 (1986) 1505–1515.
[50] J. Khalil-Allafi, A. Dlouhy, G. Eggeler, Ni_4Ti_3-precipitation during aging of NiTi shape memory alloys and its influence on martensitic phase transformations, Acta Mater. 50 (2002) 4255–4274.
[51] J. Khalil-Allafi, X. Ren, G. Eggeler, The mechanism of multistage martensitic transformations in aged Ni-rich NiTi shape memory alloys, Acta Mater. 50 (2002) 793–803.
[52] J. Michutta, C. Somsen, A. Yawny, A. Dlouhy, G. Eggeler, Elementary martensitic transformation processes in Ni-rich NiTi single crystals with Ni_4Ti_3 precipitates, Acta Mater. 54 (2006) 3525–3542.
[53] D. Schryvers, W. Tirry, S.S. Cao, Advanced TEM and SEM methods applied to 3D nano- and microstructural investigations of Ni4Ti3 precipitates in Ni-Ti (SMA), Solid State Phenom. 172–174 (2011) 229–235.
[54] A.R. Pelton, J. DiCello, S. Miyazaki, Optimisation of processing and properties of medical grade Nitinol wire, Minim. Invasiv. Ther. 9 (2000) 107–118.
[55] C.-H. Chen, Y.-C. Wang, S.-K. Wu, N.-H. Lu, Precipitation hardening by nanoscale Ti2Ni phase in high Ti-rich Ti52.6Ni46.8Si0.6 melt-spun ribbon, J. Alloys Compd. 810 (2019) 151904.
[56] A.W. Young, R.W. Wheeler, N.A. Ley, O. Benafan, M.L. Young, Microstructural and thermomechanical comparison of Ni-rich and Ni-lean NiTi-20 at.% Hf high temperature shape memory alloy wires, Shape Mem. Superelasticity 5 (2019) 397–406.
[57] J. Mentz, J. Frenzel, M.F.X. Wagner, K. Neuking, G. Eggeler, H.P. Buchkremer, D. Stover, Powder metallurgical processing of NiTi shape memory alloys with elevated transformation temperatures, Mater. Sci. Eng., A 491 (2008) 270–278.
[58] M. Carl, B. Van Doren, M.L. Young, In situ synchrotron radiation X-ray diffraction study on phase and oxide growth during a high temperature cycle of a NiTi-20 at.% Zr high temperature shape memory alloy, Shape Mem. Superelasticity 4 (2018) 174–185.
[59] P. Stadelmann, JEMS (2019). https://www.jems-swiss.ch/. (Accessed 15 February 2020).
[60] J. Frenzel, Z. Zhang, C. Somsen, K. Neuking, G. Eggeler, Influence of carbon on martensitic phase transformations in NiTi shape memory alloys, Acta Mater. 55 (2007) 1331–1341.
[61] J. Frenzel, M. Frotscher, V. Petzoldt, K. Neuking, G. Eggeler, K. Weinert, NiTi shape memory alloy metallurgy—fabrication of ingots and sputter targets,

in: SMST-2004: Proceedings of the International Conference on Shape Memory and Superelastic Technologies, ASM International, 2006, pp. 223–228.
[62] D. Schryvers, G.S. Firstov, J.W. Seo, J. VanHumbeeck, Y.N. Koval, Unit cell determination in CuZr martensite by electron microscopy and X-ray diffraction, Scripta Mater. 36 (1997) 1119–1125.
[63] Y. Kudoh, M. Tokonami, S. Miyazaki, K. Otsuka, Crystal-structure of the martensite in Ti-49.2at-percent-Ni alloy analyzed by the single crystal x-ray-diffraction method, Acta Metall. 33 (1985) 2049–2056.
[64] T.A. Sviridova, N.P. Diakonova, E.V. Shelekhov, V.P. Glazkov, Change of crystal structure of Zr2Cu after a treatment in ball mill and annealing, Poverkhnostnye Fizika, Khimiya, Mekhanika 37 (2004) 28–32.
[65] M.V. Nevitt, J.W. Downey, Family of intermediate phases having the Si2Mo-type structure, Trans. Metall. Soc. Aime 224 (1962) 195–196.
[66] M.S. El-Eskandarany, J. Saida, A. Inoue, Room-temperature mechanically induced solid-state devitrifications of glassy Zr65Al7.5Ni10Cu12.5Pd5 alloy powders, Acta Mater. 51 (2003) 4519–4532.
[67] D. Arias, J.P. Abriata, Cu-Zr (Copper-Zirconium), in: T.B. Massalski, H. Okamato, P.R. Subramanian, L. Kacprzak (Eds.), Binary Alloy Phase Diagrams, ASM International, Materials Park, Ohio, 1990, pp. 1511–1513.
[68] F. Otto, Y. Yang, H. Bei, E.P. George, Relative effects of enthalpy and entropy on the phase stability of equiatomic high-entropy alloys, Acta Mater. 61 (2013) 2628–2638.
[69] F. Otto, A. Dlouhy, K.G. Pradeep, M. Kubenova, D. Raabe, G. Eggeler, E.P. George, Decomposition of the single-phase high-entropy alloy CrMnFeCoNi after prolonged anneals at intermediate temperatures, Acta Mater. 112 (2016) 40–52.
[70] Z.M. Li, K.G. Pradeep, Y. Deng, D. Raabe, C.C. Tasan, Metastable high-entropy dual-phase alloys overcome the strength-ductility trade-off, Nature 534 (2016) 227–230.
[71] W. Steurer, J. Dshemuchadse, Intermetallics: Structures, Properties, and Statistics, Oxford University Press, Oxford, 2016.
[72] A. Takeuchi, A. Inoue, Classification of bulk metallic glasses by atomic size difference, heat of mixing and period of constituent elements and its application to characterization of the main alloying element, Mater. Trans. 46 (2005) 2817–2829.
[73] M.C. Troparevsky, J.R. Morris, P.R.C. Kent, A.R. Lupini, G.M. Stocks, Criteria for predicting the formation of single-phase high-entropy alloys, Phys. Rev. X 5 (2015) 6.
[74] G.A. Yurko, J.W. Barton, J.G. Parr, The crystal structure of Ti2Ni, Acta Crystallogr. 12 (1959) 909–911.
[75] M. Matsuda, K. Hayashi, M. Nishida, Ductility enhancement in B2-type Zr-Co-Ni alloys with martensitic transformation, Mater. Trans. 50 (2009) 2335–2340.
[76] P. Nash, C.S. Jayanth, Ni-Zr (Nickel-Zirconium), in: T.B. Massalski, H. Okamato, P.R. Subramanian, L. Kacprzak (Eds.), Binary Alloy Phase Diagrams, ASM International, Materials Park, Ohio, 1990, pp. 2889–2890.
[77] P. Nash, A. Nash, Hf-Ni (Hafnium-Nickel), in: T.B. Massalski, H. Okamato, P.R. Subramanian, L. Kacprzak (Eds.), Binary Alloy Phase Diagrams, ASM International, Materials Park, Ohio, 1990, pp. 2094–2096.
[78] A.J. Ross, T. Gheno, P.K. Ray, M.J. Kramer, X.L. Liu, G. Lindwall, B. Zhou, S.L. Shang, B. Gleeson, Z.K. Liu, A first-principles based description of the Hf-Ni system supported by high-temperature synchrotron experiments, Thermochim. Acta 668 (2018) 142–151.
[79] M.E. Kirkpatrick, D.M. Bailey, J.F. Smith, The structures of NiZr2, NiZr and their hafnium analogs, Acta Crystallogr. 15 (1962) 252–255.
[80] J.L. Murray, Cu-Ti (Copper-Titanium), in: T.B. Massalski, H. Okamato, P.R. Subramanian, L. Kacprzak (Eds.), Binary Alloy Phase Diagrams, ASM International, Materials Park, Ohio, 1990, pp. 1494–1496.
[81] S.H. Zhou, R.E. Napolitano, Identification of the B33 martensite phase in Cu-Zr using first-principles and X-ray diffraction, Scripta Mater. 59 (2008) 1143–1146.
[82] L.D.E. Subramanian P.R, Cu-Hf (Copper-Hafnium), in: T.B. Massalski, H. Okamato, P.R. Subramanian, L. Kacprzak (Eds.), Binary Alloy Phase Diagrams, ASM International, Materials Park, Ohio, 1990, pp. 1416–1419.
[83] Y. Zhong, A. Saengdeejing, L. Kecskes, B. Klotz, Z.K. Liu, Experimental and computational studies of the Cu-Hf binary system, Acta Mater. 61 (2013) 660–669.
[84] J.L. Murray, Pd-Ti (Palladium-Titanium), in: T.B. Massalski, H. Okamato, P.R. Subramanian, L. Kacprzak (Eds.), Binary Alloy Phase Diagrams, ASM International, Materials Park, Ohio, 1990, pp. 3058–3060.
[85] T. Yamamuro, Y. Morizono, J. Honjyo, M. Nishida, Phase equilibrium and martensitic transformation in near equiatomic Ti-Pd alloys, Mater. Sci. Eng., A 438–440 (2006) 327–331.
[86] L.A. Bendersky, J.K. Stalick, R. Portier, R.M. Waterstrat, Crystallographic structures and phase transformations in ZrPd, J. Alloys Compd. 236 (1996) 19–25.
[87] M.S. S.M.J. Chandrasekharaiah, K.A. Gingerich, J.A. Speed, Pd-Zr (Palladium-Zirconium), in: T.B. Massalski, H. Okamato, P.R. Subramanian, L. Kacprzak (Eds.), Binary Alloy Phase Diagrams, ASM International, Materials Park, Ohio, 1990, pp. 3068–3072.
[88] S. Hisada, M. Matsuda, K. Takashima, Y. Yamabe-Mitarai, Structural analysis and martensitic transformation in equiatomic HfPd alloy, J. Solid State Chem. 258 (2018) 712–717.
[89] S.N. B.S.R. Tripathi, The Hf-Pd (Hafnium-Palladium) system, J. Phase Equil. 16 (1995) 527–531.
[90] R.H. Woodman, B.R. Klotz, L.J. Kecskes, Observation of incongruent melting in Cu10Hf7, J. Phase Equilibria Diffus. 27 (2006) 477–481.
[91] L. Xia, K.C. Chan, S.K. Kwok, Y.D. Dong, formation of metastable phases and their effect on the glass-forming ability of Cu-Hf binary alloys, Mater. Trans. 51 (2010) 68–71.
[92] D. Porter, K.E. Easterling, M.Y. Sherif, Phase Transformations in Metals and Alloys, 3 ed., CRC Press, Boca Raton, 2009.
[93] M. Zarinejad, Y. Liu, Dependence of transformation temperatures of NiTi-based shape-memory alloys on the number and concentration of valence electrons, Adv. Funct. Mater. 18 (2008) 2789–2794.
[94] M. Zarinejad, Y. Liu, Dependence of transformation temperatures of shape memory alloys on the number and concentration of valence electrons, in: H.R. Chen (Ed.), Shape Memory Alloys: Manufacture, Properties and Applications, Nova Science Publishers, New York, 2010, pp. 339–360.
[95] J.M. Ball, R.D. James, Proposed experimental tests of a theory of fine microstructure and the two-well problem, Phil. Trans. Roy. Soc. Lond. 338 (1992) 389–450.
[96] R.D. James, Z. Zhang, A way to search for multiferroic materials with “unlikely” combinations of physical properties, in: A. Planes, L. Mañosa, A. Saxena (Eds.), Magnetism and Structure in Functional Materials, Springer, Berlin/Heidelberg, 2005, pp. 159–175.
[97] J. Cui, Y.S. Chu, O.O. Famodu, J. Hattrick-Simpers, R.D. James, A. Ludwig, S. Thienhaus, M. Wuttig, Z. Zhang, I. Takeuchi, Combinatorial search of thermoelastic shape-memory alloys with extremely small hysteresis width, Nat. Mater. 5 (2006) 286–290.
[98] J. Frenzel, On the importance of structural and functional fatigue in shape memory technology, Shape Mem. Superelasticity 6 (2020) 213–222.
[99] D. König, P. Frowein, A. Wieczorek, J. Frenzel, S. Hamann, G. Eggeler, A. Ludwig, Composition, constitution and phase transformation behavior in thin-film and bulk Ti–Ni–Y, Shape Mem. Superelasticity 3 (2017) 49–56.
[100] N. Ronald, B. Tiffany, P. Santo, NiTi-based high-temperature shape-memory alloys, in: W.O. Soboyejo, T.S. Srivatsan (Eds.), Advanced Structural Materials, CRC Press, 2006, pp. 145–186.
[101] C. Chluba, W. Ge, T. Dankwort, C. Bechtold, R.L. De Miranda, L. Kienle, M. Wuttig, E. Quandt, Effect of crystallographic compatibility and grain size on the functional fatigue of sputtered TiNiCuCo thin films, Phil. Trans. Roy. Soc. Lond. 374 (2016) 20150311.